The Design, Construction and Characterization of a Low Temperature Scanning Hall Probe Microscope

by

Nigel David

B.Sc, Simon Fraser University, 2004

A THESIS SUBMITTED IN PARTIAL FULFILLMENT
OF THE REQUIREMENTS FOR THE DEGREE OF
MASTER OF SCIENCE
in the Department
of
Physics

SIMON FRASER UNIVERSITY
Spring 2007

APPROVAL

Name: Nigel David

Degree: Master of Science

Title of thesis: The Design, Construction and Characterization of a Low Temperature Scanning Hall Probe Microscope

Examining Committee: Dr. Karen Kavanagh
Chair

Dr. David M. Broun, Senior Supervisor
Assistant Professor, Department of Physics, SFU

Dr. J. Steven Dodge, Supervisor
Assistant Professor, Department of Physics, SFU

Dr. Jeffrey McGuirk, Supervisor
Assistant Professor, Department of Physics, SFU

Dr. John Bechhoefer, Internal Examiner,
Professor, Department of Physics, SFU

Date Approved: January 17, 2007

Abstract

Scanning Hall probe microscopy, which uses a Hall-effect sensor to non-invasively image magnetic fields at the surface of samples, is a powerful tool in condensed matter physics that can be used to study magnetism on mesoscopic length scales. The work done for this thesis was in the design, construction and characterization of a low temperature scanning Hall probe microscope for our lab. We have based some parts of our design, such as the 500 μm range piezo scanner, on other microscopes in the field. However, components such as the "double-gimbal" rotation stage for the sensor, and the sample stage with capacitive touch-down sensor and thermal control, are unique to our design. Already the first of its kind in Canada, with the intended addition of a scanning near-field optical probe to the same scan-head as the Hall probe, this microscope will have unique features not available in any other lab.

Acknowledgments

First and foremost I would like to thank my supervisor David Broun for giving me the opportunity to build such a cool low-temperature experiment for my Masters project. The learning environment he provided to achieve this task would be hard to find anywhere else, and as a result I've come away with many skills that will surely help me in the future. He has been a mentor to me both in and out of the lab, and his level of expertise and positive energy are things that I will strive for in my career. Along with Dave, three other exceptional physicists including Jeff McGuirk, Steven Dodge and John Bechhoefer formed my examining committee. I would also like to thank them for their feedback on my thesis work.

In my time as a member of Dave's research group I have seen the lab space get transformed from a practically empty room, with only a tool box and a dilution fridge in a crate, to a proper physics laboratory full of low-temperature experiments and bustling with activity. I was lucky enough to be a part of the first generation of grad students in the Broun lab, which included Wendell Huttema, Xiao Qing, and Ricky Chu, who helped make this transformation possible. These guys were great to work with; the type of guys who will drop anything to help you out. This can also be said about Pat Turner, the post-doc in our group who I worked closely with on many aspects of this project. I have learned a great deal from him in low-temperature experimental design, and experimentation in general. His patience and sense of humor made working with him a pleasure.

The construction of the scanning magnetic microscope for this project was not all carried out on my own of course, and I would like to thank the undergraduate group members Adam Schneider (now a Masters student at McGill), and Taras Chouinard

for developing software and hardware for the scanner. Not only were Adam's software contributions central to the operation of the microscope, his philosophizing always kept the lab conversation interesting. Taras' work developing the coarse positioning system will soon set this microscope apart from the rest and maybe one day his positioners will be found in other labs. There are many other students in the department who gave me technical advice and moral support during this project, and for that I thank you all very much.

The magnetic imaging that I carried out during the last part of my thesis work was only possible with the state-of-the-art Hall probes kindly provided by Clifford Hicks, a PhD candidate in Kathryn Moler's group at Stanford University. I would like to thank Clifford, Kathryn, and Janice Guikema for their help in bringing us up to speed in this field of research.

My time here as a graduate student was made much easier with help from the SFU support staff. Much thanks goes to Brian Gormann, Vic Allen, and Ken Myrtle from the physics department, who have always been around to help with technical issues, no matter how big or small; James Shoults and Howard Proulx of the SFU machine shop for their enthusiasm in machining our intricate microscope parts; the guys in the SFU electronics shop; Bill Woods of the engineering clean-room for his many patient attempts at wire-bonding to our Hall probes; and Sada Rangnakar, Candida Mazza, Margaret van Soest and the rest of excellent physics administrative staff.

Finally, I would like to thank my family for their ongoing love and support throughout my educational journey. I am so lucky to have such a supportive family. My wife Danielle in particular has been there for me every step of the way, and has been a huge source of encouragement and energy despite having the full time job of mothering our beautiful sons Tyler, Dylan and Kaelin. Thank-you so much.

Contents

Approval ii

Abstract iii

Acknowledgments iv

Contents vi

List of Figures ix

1 Introduction 1

1.1 Scanning microscopy 2

1.2 Overview of scanning magnetic imaging techniques 6

1.2.1 Magnetic force microscopy 6

1.2.2 Scanning SQUID microscopy 8

1.2.3 Scanning Hall probe microscopy 10

1.3 Magnetic imaging and spatial resolution 12

1.4 Vortex imaging in scanning Hall probe microscopy 14

1.4.1 Type II superconductors and the vortex state 15

1.4.2 Scanning Hall probe studies of high T_c cuprates 18

2 Sub-micron scanning Hall probes 23

2.1 The Hall effect 24

2.2 Theoretical limits on Hall probes 25

2.2.1 Magnetic field sensitivity 25

2.2.2 Fundamental limits on length scales . . . 28
2.3 GaAs/AlGaAs Hall probes . . . 29
2.3.1 Clifford Hicks' 100 nm-scale Hall probes . . . 30

3 Mechanical design of the SHPM **37**
3.1 Overview of the design . . . 38
3.2 Sample stage with touch-down sensor . . . 40
3.3 Scanning stage . . . 42
3.3.1 Large area x, y scanner . . . 42
3.3.2 Fine z motion . . . 47
3.3.3 Fine motion calibration . . . 47
3.3.4 Double-gimbal angular positioner . . . 55
3.3.5 Flat surface topography . . . 57
3.4 Coarse motion . . . 58
3.4.1 Three axis Attocube coarse motion system . . . 58
3.4.2 Capacitive position read-out . . . 60
3.5 Superconducting magnet . . . 62

4 Thermal Design **64**
4.1 Cryostat . . . 64
4.2 Sample thermal stage . . . 66
4.2.1 Heat transfer from the sample stage . . . 67
4.2.2 Sample thermometry and heating . . . 68
4.3 SHPM insert design . . . 71

5 Scanner electronics and software **73**
5.1 Scanner electronics . . . 73
5.2 Thermometer and heater electronics . . . 74
5.3 Attocube electronics . . . 75
5.4 Capacitive sensor electronics . . . 75
5.5 Hall probe electronics . . . 75
5.6 Scanning software . . . 76

6 Preliminary results and discussion 77

Bibliography 81

List of Figures

1.1 Schematic of typical scanning magnetic microscope systems 2
1.2 Flux sensitivity versus sensor size for SQUIDs and Hall probes 5
1.3 High resolution MFM tip and image of a hard disk. 7
1.4 Recent 100 nm-scale low temperature scanning Hall probe and image of vortices 11
1.5 Spatial resolution of SQUIDs and Hall probes 13
1.6 Alignment procedure for the Hall sensor 13
1.7 Field versus temperature phase diagram for type II superconductors . 17
1.8 Magnetic field profile of a single vortex 17
1.9 The unit cell for YBCO 19
1.10 Phase diagram for the high T_c cuprates 20

2.1 Schematic of a Hall sensor 24
2.2 GaAs/AlGaAs 2DEG heterostructure cartoon and band energy 31
2.3 Wirebonded 150 nm Hall probe with SEM close-up 32
2.4 Hicks' Hall probe characterization plots 34
2.5 Timetrace plots for various gate voltages 35

3.1 CAD drawing of the SHPM mechanical design 38
3.2 Picture and CAD drawing of the sample thermal stage 41
3.3 Pictures of the scanning stage 42
3.4 The design of the large area scanner 44
3.5 Fine z motion stage design 47
3.6 Schematic of topography procedure for calibration of the scanner . . . 48

3.7 z motion calibration plot 49
3.8 Line topograph of pattern on silicon 50
3.9 Tools for lateral calibration of the scanner 51
3.10 Room temperature y direction calibration using a silicon grating . . . 52
3.11 Low-temperature lateral calibration plot 53
3.12 Double-gimbal rotation stage design 55
3.13 Plot showing sensor angle adjustments 56
3.14 Plot showing a large range topograph of a clean sapphire surface . . . 58
3.15 Picture of the three axis Attocube sample positioning system 59
3.16 Attocube position sensor retrofit design 60
3.17 Plot showing the calibration of the capacitive position sensor 61
3.18 Pictures of the SHPM and the superconducting magnet 63

4.1 A picture of the cryostat we built for the SHPM. 65
4.2 Thermal design of the sample stage 68

5.1 A schematic of the electronics for the SHPM. 74

6.1 Picture of the scanner with Hall probe mounted. 78
6.2 Scanning Hall probe image of a floppy disk at 77 K 79

Chapter 1

Introduction

The bulk of the work done for my Masters project has been in the design, construction, and characterization of a low temperature scanning Hall probe microscope (SHPM). This is the first instrument of its kind here at SFU, or even in Canada for that matter, and the first part of this thesis (Chapters 1 and 2) is devoted to background on the technique and on the Hall probes used in scanning Hall probe microscopy. This will serve to give those entering the field, particularly new graduate students, useful information prior to or during their projects using the SHPM. Having said that, this introductory chapter focuses on how scanning Hall probe microscopy, when compared to other techniques, emerges as a powerful tool in experimental mesoscopic physics, one of the frontiers in condensed matter physics. Some of the magnetic and superconducting materials of interest are also discussed here, with an emphasis on type II superconductors and the vortex state, in which many interesting magnetic phenomena of theoretical importance arise. Chapter 2 is about Hall probe fundamentals and technology. Included here is a discussion of the fundamental limits on flux sensitivity and spatial resolution for Hall probes, followed by a description of the state-of-the-art 150 nm GaAs/AlGaAs Hall probes we have been provided by Clifford Hicks, a Stanford PhD candidate, to get started with. Chapter 3 starts off the second part of the thesis detailing the mechanical design of our SHPM and its characterization. Chapter 4 describes the thermal design of our SHPM, an important element for an experiment routinely being run at 4.2 K, and Chapter 5 is on the electronics and software used

to run the SHPM. Finally, to demonstrate the operation of the SHPM we have built, Chapter 6 shows an image of magnetic bits on a floppy disk taken with the SHPM. This is followed by a summary of the project, highlighting some of the issues that caused considerable difficulty, and the insight that I ultimately gained from them.

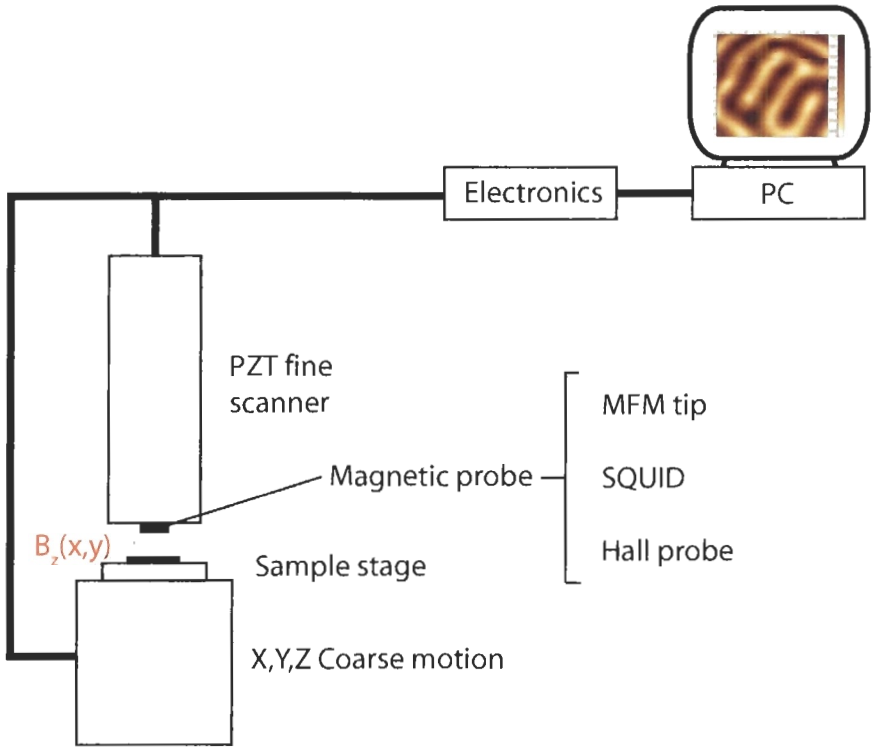

Figure 1.1: A schematic of a typical scanning magnetic microscope. For cryogenic use it would be mounted in a helium cryostat or dilution refrigerator.

1.1 Scanning microscopy

The proliferation of scanning microscopy began in the early 1980's with the invention of the scanning tunneling microscope (STM) by Binnig and Rohrer [1], and was soon followed by the development of another well known instrument, the atomic force microscope (AFM) [2], invented in 1986. Since then, many other scanning probe

microscopy techniques have arisen, all sharing the same basic operating principle, depicted schematically in Figure 1.1: a microscopic sensor, mounted on a piezo scanner, is scanned over a grid of points at the surface of a sample, locally measuring a physical property at each point to create an image. The range of sensors available, and the relatively compact size of the apparatus, makes the scanning probe microscope a very powerful and productive tool in condensed matter physics.

The scanning microscope I designed and built for this thesis uses a Hall probe as a local magnetic sensor to image magnetic fields at the surface of samples. With the intended addition of a near-field scanning optical probe to the same scan head as the Hall probe, our microscope has the potential to be a unique scientific instrument worldwide. The primary focus of the research done with this microscope will be on mesoscopic superconductivity and magnetism, where 'mesoscopic' describes length scales that are larger than atomic dimensions, but still small enough so that the physical behaviour can be strongly influenced by the laws of quantum mechanics. Magnetic vortices in type II superconductors are naturally quantized structures that exist in the mesoscopic regime, and will thus be the subject of much study with this microscope. Furthermore, with the near-field optical probe, one will be able to "write" superconducting nanostructures by persistent photodoping of otherwise insulating cuprates, and then immediately image their magnetic properties with the Hall probe; no such system exists today so there are many opportunities for research here.

The range of applications for this microscope is not restricted to magnetic vortices or mesoscopic phenomena. Innovations in piezoceramic scanner design [3] have allowed for low temperature scan ranges of ~0.5 mm, and with Hall probes now offering sub-micron spatial resolution, the scope of applications encompasses magnetic structures existing on length scales spanning three orders of magnitude. Much of the most interesting physics to researchers today is, however, on the small side of this spectrum, which includes mesoscopic phenomena, so continued effort is being put into Hall probe design and fabrication to make smaller and more sensitive devices.

Hall probes are now being fabricated down to the 100 nm-scale [4]; combined with flux sensitivities of around 10 $\mu\Phi_0/\sqrt{\text{Hz}}$, and a broad operating temperature and

field range, scanning Hall probe microscopy has emerged as one of the key players in scanning magnetic imaging. The other scanning magnetic imaging techniques are magnetic force microscopy (MFM), and scanning SQUID microscopy. These techniques each have their own advantages and are compared in detail in the following section. Although the STM was used early on by Hess and coworkers to be the first scanning probe microscope to image magnetic vortices in type II superconductors [5], it does not measure the magnetic field at all, but rather the local density of states at the surface of the sample, which is also correlated with vortex phenomena. This type of STM imaging is called scanning tunneling spectroscopy, and is still a very useful tool to study vortices and unconventional superconductivity. Conventional scanning tunneling *microscopy* has nonetheless played a central role in scanning magnetic microscopy, where it is often used to guide the magnetic probe along the surface of the sample at a constant height.

Since scanning probe microscopy techniques rely on the probe being at the surface of the sample, some sort of topographic feedback is essential. Topography is the primary domain of the STM and the AFM, so they are often part of a scanning magnetic microscope. The STM works by scanning an atomically sharp metallic tip biased with a small voltage, over a grounded conducting sample. As the tip gets closer to the surface, the quantum tunneling current increases exponentially. In constant current, or topography mode, the tunneling current is fed back to the height control of the tip, which is adjusted during the scan so that the current remains constant. These heights are recorded, and the height map represents a surface of constant conduction electron energy. For this to be incorporated into a scanning magnetic microscope, the sensor, either Hall probe or superconducting quantum interference device (SQUID) has a tunneling tip microfabricated alongside the device. The AFM is sensitive to the atomic forces at the surface of the sample acting on a tip at the end of a cantilever. It maps the surface by adjusting the height of the cantilever as it is scanned so that the force remains constant. This is combined with magnetic microscopy when the tip is coated with a ferromagnetic material, making it sensitive to magnetic forces as well. Now it is a magnetic force microscope.

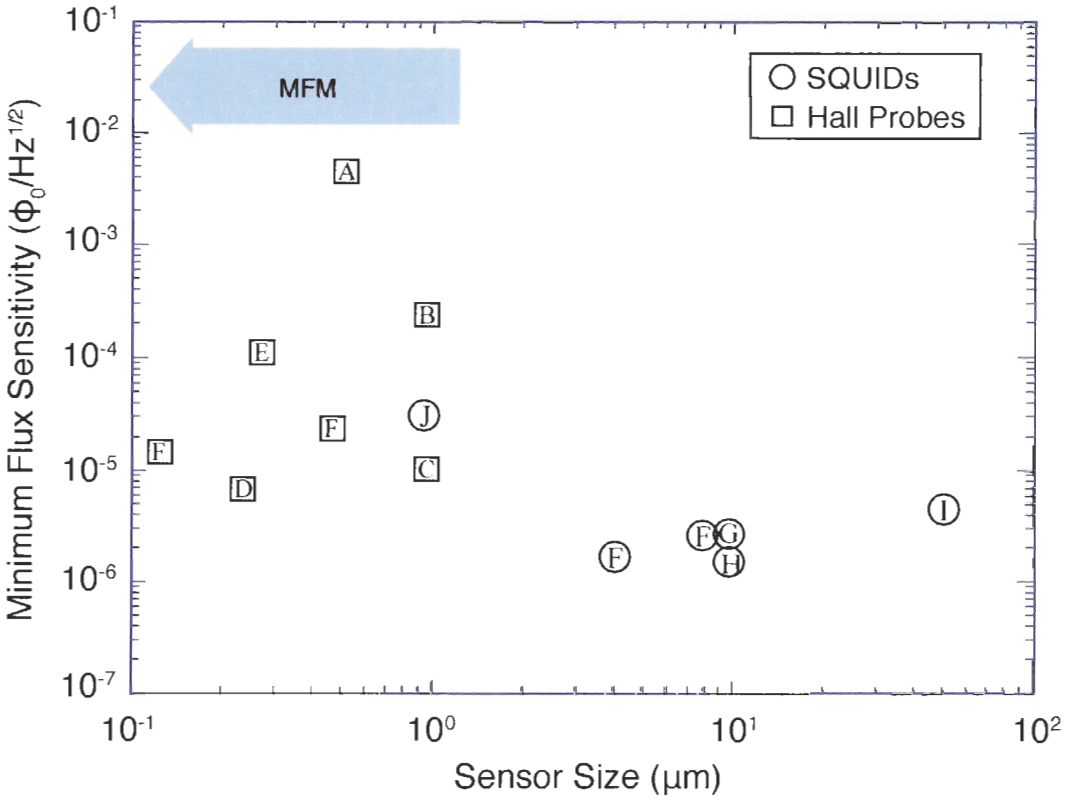

Figure 1.2: A plot showing the evolution in performance of mesoscopic magnetic probes in recent years from the literature, in terms of their minimum flux sensitivity (white noise floor) versus sensor size. Hall probes: (A) Chang et al. [6], (B) Davidović et al. [7], (C) Oral et al. [8] at 77 K, (D) Oral et al. [9] at 77 K, (E) Grigorenko et al. [77 K; GaAs/InAs/GaSb], (F) Moler research group. SQUIDs: (F) Moler research group, (G) Vu et al. [10], (H) Kirtley et al. [11], (I) Stawiasz et al. [12], and (J) Hasselbach et al. [13] [Al]. MFM sensors do not have as good flux sensitivity, but can have spatial resolution of ~20 nm using carbon nanotube tips [14]. Unless otherwise noted: $T \leq 5$ K, Hall probes were GaAs/AlGaAs, and SQUIDs were Nb. Figure is adapted from Ref [15].

1.2 Overview of scanning magnetic imaging techniques

Imaging microscopic variations of magnetic fields at surfaces can be done by various techniques and Bending gives a thorough overview of those that are available for the investigation of superconductors [16]. Among them are three techniques in particular that involve scanning magnetic probe microscopy: MFM, scanning SQUID microscopy, and scanning Hall probe microscopy. These techniques are all employed at a state-of-the-art level by the Moler research group at Stanford University to study vortices in high temperature superconductors, and as such have been discussed together extensively in their publications. Here I give an overview of the techniques, highlighting how they compare in the following key areas:

- spatial resolution
- magnetic field, and flux sensitivity
- invasiveness
- possibility of quantitative and interpretable measurement
- operating temperature range

How they perform in these areas determines the scope of applications the technique can be used for.

1.2.1 Magnetic force microscopy

Magnetic force microscopy, MFM, uses an AFM cantilever with a magnetic tip to measure the force between the tip and the sample magnetic field as it is scanned across the surface. The quantity measured is $\mathbf{F} = \int_{tip} \nabla(\mathbf{M} \cdot \mathbf{B}) dV$, where $\mathbf{M}$ is the magnetization of the tip, and $\mathbf{B}$ is the magnetic field; thus it is not straightforward to interpret an MFM image in terms of magnetic field, since it is convolved with $\mathbf{M}$, which is hard to characterize. The main strength of MFM is its spatial resolution,

which is currently better than for SQUIDs and Hall probes, occupying a spatial region of the plot in Figure 1.2 not yet reached by the other techniques. Spatial resolution in MFM depends on the tip size, shape, and its height above the surface of the sample. An example of a commercially available MFM tip is shown in Figure 1.3(a), which has a thin magnetic coating and is reported to have a tip diameter of < 50 nm[1]. Recent innovative MFM probes, including iron-filled [17] and metal coated multiwalled carbon nanotubes [14], are likely to bring MFM resolution to $\sim$10 nm.

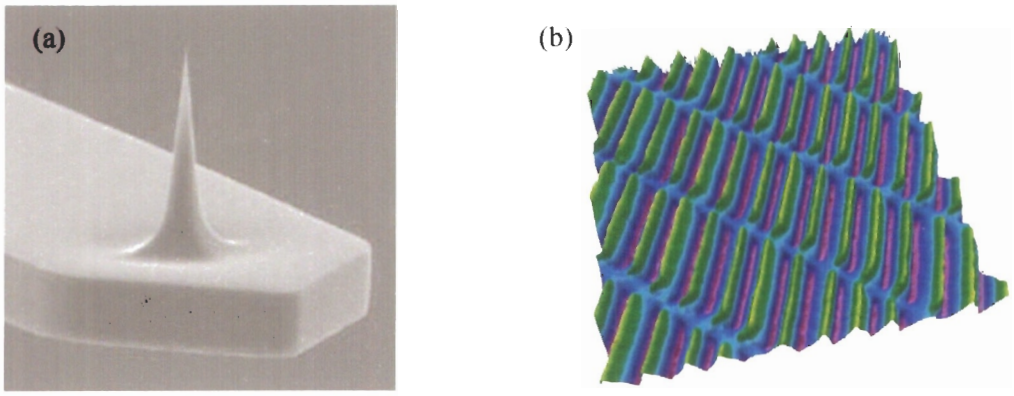

Figure 1.3: (a) Optical microscope image of a high resolution MFM tip. Courtesy of NanoScience Instruments. The tip diameter is < 50nm. (b) A 20×20 μm^2 MFM image of a hard disk. Imaged with an Asylum Research MFP-3D Atomic Force Microscope, courtesy Asylum Research, Santa Barbara, CA.

Not only does MFM have unmatched spatial resolution, it also requires no special sample preparation nor does the probe need to be at low temperatures to operate. These qualities make the applications and possibilities for this technique quite plentiful. The most obvious applications are for nanomagnetic materials [18] and magnetic storage media; in fact, MFM has been the standard for measuring the dimensions of magnetic bits, and for characterizing the bit structure irregularities on hard disks.

[1]This image is taken from the NanoScience Instruments website.

Figure 1.3 shows a 20×20 μm^2 MFM image of a conventional hard disk with tracks of bits written on it. Perpendicular magnetic storage, with bit sizes of ∼20 nm [19], continues to place increased demand on MFM and its new probes for the characterization of these new media.

A feature of MFM, which is often undesirable, is its invasiveness: the magnetic field of the tip makes a non-negligible perturbation of the structure under study. This may seem to limit the objective investigation capabilities of the technique to hard magnetic structures; however, it is taken advantage of in the investigation of things such as vortex pinning forces, and vortices have even been dragged around to create structures out of them[2]. MFM has also recently been used to control the magnetic states of ferromagnetic nanodots [18].

1.2.2 Scanning SQUID microscopy

The Superconducting QUantum Interference Device is currently the most sensitive detector of magnetic flux, with a sensitivity down to ∼0.3 $\mu\Phi_0/\sqrt{\text{Hz}}$, where Φ_0 is the superconducting flux quantum $hc/2e$. The device consists of a superconducting loop with two Josephson junctions and measures the flux ($\Phi = \int_{loop}\mathbf{B}\cdot\mathbf{da}$) threading the loop no matter how the field is distributed inside it. This makes for an interpretable measurement, with results that are quantifiable, meeting some of the criteria for scanning magnetic microscopy. SQUID pick-up loops can be made very large to achieve unrivaled magnetic field sensitivity; however, for scanning SQUID microscopy, good spatial resolution demands that the devices be made very small, which is technically difficult due to their complex design. The summary article by Kirtley in 2002 gives an overview of the advances in and recent uses of mesoscopic scanning SQUIDs [20]. Scanning SQUIDs are typically made with niobium, the material used for most superconducting electronics, and the best flux sensitivity reported is slightly above 1 $\mu\Phi_0/\sqrt{\text{Hz}}$ for 4-10 μm pick-up loops. The limitations for SQUIDs lie in their spatial resolution, operating temperature and field range.

[2]Images of this can be found on the Centre for Probing the Nanoscale (CPN) website, www.stanford.edu/group/cpn/index.html

Scanning SQUID microscopy is a good technique when high field sensitivity is called for and high spatial resolution is not. Superconducting vortices with low spatial density are therefore ideal systems to study with this technique. In 1996, Kirtley and coworkers used a 4 μm SQUID (the state of the art for its time) to observe half-integer flux quantization occurring on grain boundaries of the high T_c superconductor $YBa_2Cu_3O_{7-\delta}$ grown on a tricrystal substrate [21]. They write that "half-integer flux quantization is a powerful tool for probing the symmetry of the superconducting gap in both $YBa_2Cu_3O_{7-\delta}$ and other unconventional superconductors". A more recent SQUID design, from Martin Huber of CU, Denver and Per Björnsson then of Stanford University [22], is more sophisticated. Although still 4 μm in size, it includes an outer loop, which is used to apply a local field to the sample allowing for scanning susceptometry to be carried out, as well as for the manipulation of vortices [23]. Björnsson writes in his 2005 thesis that "to make smaller SQUIDs, continuing work on integrating e-beam lithography (or some other higher-resolution processing method) in the process will be necessary."

The size of a SQUID is not only limited by the technical difficulty of fabricating these devices, but more fundamentally by the penetration depth, λ, of the superconducting material used. A fundamental quantity in superconductivity, λ describes the length scale over which a magnetic field penetrates the material. When the linewidth of the superconducting pick-up loop approaches λ, the squid loses sensitivity [22]. A typical value for λ in thin- film Nb, the most commonly used material for superconducting electronics, is 90 nm. In practice, this likely limits the effective size of a SQUID to a few hundred nanometers.

Different materials have different penetration depths, so other superconductors may be explored with small λ to make smaller devices. But besides the fabrication challenges other materials may present, these materials would have a different superconducting transition temperature, T_c. For niobium, T_c = 9.3 K and it is 1 K for aluminum, another material used for SQUIDs. Since the SQUID pick-up loop must be superconducting, its operation is restricted to temperatures below the T_c of the material used, which greatly limits the versatility of the technique in general. To broaden their temperature range, high T_c materials can be used for SQUIDs, but

their sensitivity is about an order of magnitude worse than for low-T_c SQUIDs with equivalent spatial resolution [15].

The operation of a SQUID is affected by the magnetic field it is in, causing flux to be trapped, and as such, its use is limited to low fields. The electromagnetic fields from the sensor itself however, are relatively weak, having little effect on the sample, making the technique non-invasive.

1.2.3 Scanning Hall probe microscopy

Hall probes are direct magnetic field sensors based on the Hall effect: when a current is exposed to a perpendicular magnetic field, the electrons are deflected to one side by the Lorentz force, thereby inducing a transverse voltage that is directly proportional to the magnetic field. Generally speaking, a Hall probe device consists of a cross of conducting material, where the active region (sensor) is the junction of the cross. A bias current is passed through the cross in one direction, while the transverse voltage is measured across the perpendicular direction.

Hall probes are non-invasive, having a self field of only ~0.4 mG [15], and can be made much smaller than SQUIDs, and almost as small as MFM tips. These attributes, as well as their broad operating temperature and field range make Hall probes an attractive choice for scanning magnetic microscopy. They have likewise led to a significant amount of development in Hall probe technology in recent years. Clifford Hicks of the Moler research group at Stanford University has been a part of this effort during his PhD work, fabricating state-of-the-art low-temperature Hall probes from GaAs/AlGaAs 2-dimensional electron gas heterostructures with lithographic sizes down to 80 nm and sensitivity of a few Gauss [4]. Although in its early stages, a collaboration has developed between the Moler group and ours; Clifford Hicks has been kind enough to give us three 150 nm Hall probes to use in our SHPM.

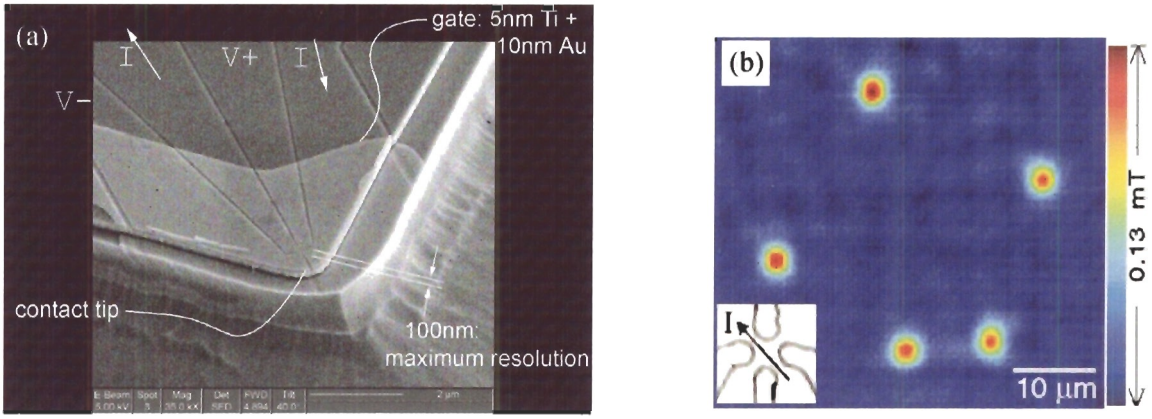

Figure 1.4: Low-temperature scanning Hall probes can be made as small as ∼100 nm, like the GaAs/AlGaAs probe in (a) fabricated by Clifford Hicks of Stanford University. Image courtesy of Clifford Hicks [24]. (b) Scanning Hall probe microscopy image of magnetic vortices in $YBa_2Cu_3O_{6+x}$. Image courtesy of Janice Guikema [15]. The image was taken with a different Hall probe from that in part (a).

Low-temperature scanning Hall probe microscopy with a GaAs/AlGaAs Hall probe was demonstrated as early as 1992 by Chang et al. [6]. They used a Hall probe with an effective size of ∼0.35 μm to image individual vortices in high T_c materials and superconducting circuits. Since then, the probes have become smaller and more sensitive, with Moler's group at Stanford being at the forefront of this effort. The evolution of the GaAs/AlGaAs Hall probe is seen in Figure 1.2, showing a plot of flux sensitivity vs. sensor size for Hall probes and SQUIDs. GaAs/AlGaAs is the material of choice for low-temperature Hall probes due to low carrier density and high mobility in the 2DEG, resulting in a high Hall coefficient and low Johnson noise for the device.

These devices are simpler in their geometry than SQUIDs, and can thus be made smaller than SQUIDs with current fabrication techniques. A fundamental limit on size, however, occurs when the Hall cross gets much smaller than the mean-free path of the charge carriers. In this case, known as the ballistic limit, the carriers move ballistically through the region, following deterministic classical trajectories that are

curved due to the Lorentz force. The problem arises when the corners of the Hall cross are rounded, which in practice they are, and multiple collisions with these corners quickly leads to chaotic trajectories of the charge carriers. In this situation the charge carriers explore the semiclassical phase space at an exponential rate, randomizing the probability that they will leave via the left or right lead, and the Hall effect is said to be quenched. To make sensors that approach the size of MFM tips, while avoiding Hall effect quenching, other materials and techniques may have to be sought. More details on GaAs/AlGaAs Hall probes, and how the fundamental properties of a material affect the noise floor and minimum size of these devices will be discussed in greater detail in the following chapter.

1.3 Magnetic imaging and spatial resolution

Some magnetic domain structures, such as perpendicular bits on recording media, can be modeled in two dimensions as mesoscopic magnetic dipoles. In order to properly image these dipoles with a magnetic sensor, the sensor must not be too big, otherwise the field will in large part cancel out within the sensor.

Spatial resolution in scanning SQUID or Hall probe microscopy is not simply determined by the size of the probe size s, but also by the height h of the probe from the surface of the sample. Even as you go short distances away from the surface of the sample, the magnetic field distribution changes rapidly from what it was inside the sample, therefore limiting ones ability to resolve surface magnetic features by scanning a magnetic sensor at too great a height. The xy spatial resolution scales roughly as $\sqrt{s^2 + h^2}$, so there is no point having an extremely small sensor unless it can be brought correspondingly close to the sample.

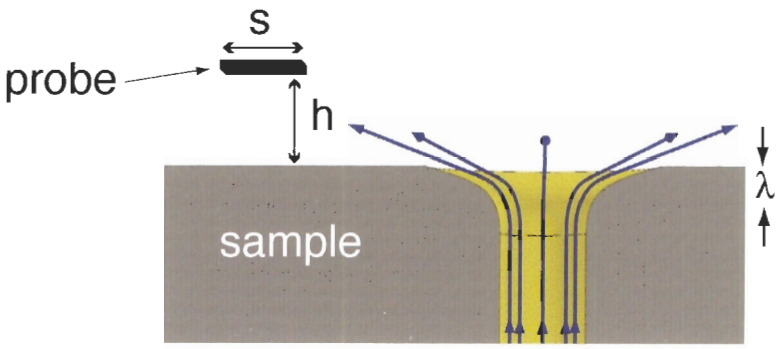

Figure 1.5: Cartoon of a magnetic sensor above a superconducting vortex. The field of a vortex above a superconductor can be modeled as that of a magnetic monopole situated a distance λ beneath the surface [25]. Spatial resolution of SQUIDs and Hall probes scales roughly as $\sqrt{s^2 + h^2}$ so it is not only important to have a small sensor, but that it be very close to the sample as well.

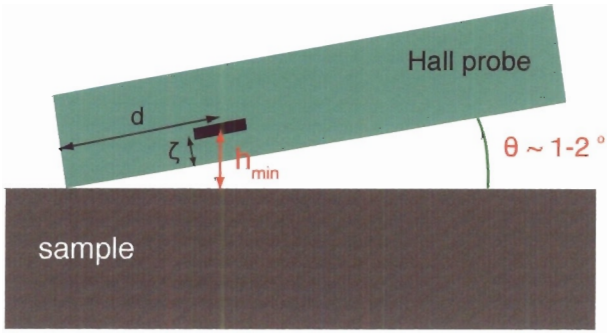

Figure 1.6: Alignment of Hall probe to obtain the minimum sensor height h_{min} for optimal spatial resolution.

To achieve optimal spatial resolution with SQUIDs and Hall probes the sensor area must be brought very close to the surface when scanning. Since these devices are fabricated on chips, the sensor is fabricated very near the end of the chip, so that with careful chip alignment, the sensor can be brought as close as possible to

the sample. Shown in the schematic of Figure 1.6 is the technique used to do this. The probe-chip is set at a shallow angle ∼1-2° relative to the sample so that the end with the sensor touches first. The sensor is at its closest to the surface of the sample when this end is just touching. If the sensor is on the surface of the chip but set back by a distance d from the contact tip, then the minimum height of the sensor is $h_{min} = d\sin\theta \sim d\theta$. For SQUID the device *is* typically fabricated on the surface of the chip, but in GaAs/AlGaAs Hall probes, the sensor is fabricated on a 2DEG that is embedded in the heterostructure, so for these probes

$$h_{min} = d\sin\theta + \zeta\cos\theta,$$

where ζ is the depth of the 2DEG. Hall probe 2DEGs can be as shallow as 39 nm, as with the most recent devices fabricated by Hicks [4]. These Hall probes also include a deep etch to form a contact tip, so that with proper polishing of the chip, this tip touches down first and d_{min} ∼1 μm. With these numbers, and if the chip is aligned at a 1° angle, we can use the above equation to determine the minimum sensor height for our 150 nm probes is h_{min} ∼60 nm. This is incredibly close, and in practice it would rarely be that good, but it means that in theory, the spatial resolution of these probes is almost limited by the size of the probe and not by the height. This is a particularly important development should future Hall crosses become smaller.

1.4 Vortex imaging in scanning Hall probe microscopy

Up to this point in the thesis, several figures have depicted magnetic vortices without much mention of their importance. A vortex is the fundamental magnetic entity in a superconductor and consists of a quantized tube of magnetic flux, Φ_0, surrounded by a whirlpool of supercurrent. The nucleation and motion of vortices are physical processes of primary importance, as together they determine the macroscopic behaviour and technological utility of superconductors. As discussed in the previous section, magnetic vortices in superconductors can be imaged by all three techniques; however, the study of vortices is particularly conducive to scanning Hall probe microscopy, due to the technique's non-invasiveness, high spatial and field resolution, and broad

temperature range. Furthermore, the study of vortices with scanning Hall probe microscopy may help uncover the highly sought after mechanism at work in the high temperature superconductors.

The imaging of individual vortices with a SHPM has been used to measure theoretically important quantities in the high T_c cuprates since 1992 [6] and has more recently been used to set a semi-quantitative upper limit on the energy scale for a theory of spin-charge separation (SCS) formulated by Senthil and Fisher (2000) [26]. Before describing these studies in further detail however, as well as a new experiment to be carried out with our microscope to further test for SCS, I will give a brief theoretical introduction to type II superconductors, the group of superconductors of which the high T_c cuprates are a part.

1.4.1 Type II superconductors and the vortex state

Type II superconductors were discovered in the mid fifties when the critical fields of carefully grown thin films were being studied by Abrikosov and colleagues [27]. They realized that the phase transitions did not agree with what was predicted by the celebrated Ginzburg-Landau (GL) theory of superconductivity proposed just a few years earlier [28]. In this theory, the material properties enter the equations as a single parameter $\kappa = \lambda/\xi$, made up of the two characteristic length scales from the microscopic Bardeen Cooper Schrieffer theory: λ is the penetration depth describing the length scale over which magnetic fields penetrate the superconductor, and ξ is the coherence length, the length scale over which the superconducting order parameter changes. It turned out that the films being studied had large values of κ, which according to GL theory led to a negative surface energy between the superconducting and non-superconducting regions in the intermediate state. This unlikely scenario had not been a priori considered by Ginzburg and Landau, whose theory seemed to explain beautifully the phase transitions of the materials studied up to that point.

Abrikosov went on to show that using the large κ in GL theory not only led to the negative surface energy but also to the second order magnetic phase transitions

to the normal state observed in the earlier experiments. Furthermore, he showed analytically that for a range of fields superconductivity coexists with "normal" material to form an exotic vortex lattice state (see Figure 1.7). Due to their unique properties, Abrikosov called these materials "superconductors of the second group". The vortex state was subsequently confirmed experimentally with the Bitter decoration technique, and these materials became known as type II superconductors. They are characterized by having $\kappa > 1/\sqrt{2}$. Having been first thought of as exotic, virtually all new superconducting compounds discovered since the early 1960s, including heavy fermion, organic, and high temperature (high-T_c) cuprate superconductors, are type II. Their magnetic properties proved to be very interesting and have made possible the application of superconducting materials in high field environments such as for MRI magnets.

Unlike conventional type I superconductors, type II materials have a so-called "mixed state" where for a range of fields the flux penetrates the material in an array of quantized bundles (vortices), interacting to form what is known as the Abrikosov Flux Lattice. The field vs. temperature phase diagram for type II materials is shown in Figure 1.7. The mixed state is actually broken up into two parts for the high T_c cuprates. For low fields between H_{c1} and H_{c2}, the vortices are fixed in place and form a "solid", and for higher fields within that range the vortices go into a liquid phase where the vortices can get pulled around by the field. When the field reaches H_{c2} superconductivity is destroyed.

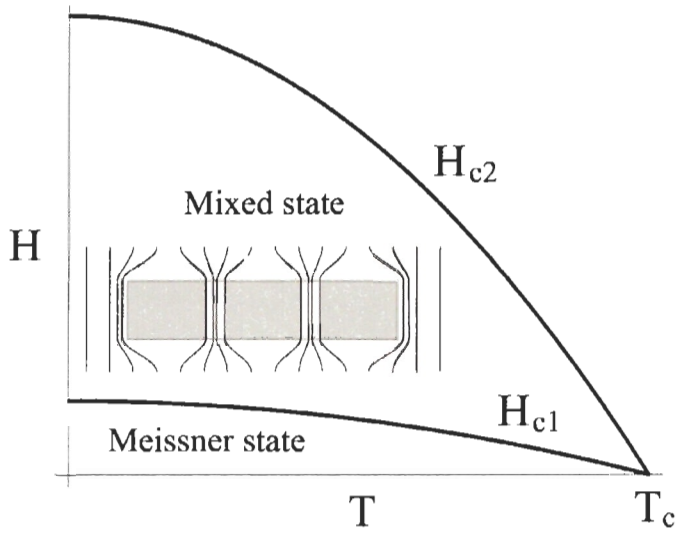

Figure 1.7: (a) Field versus temperature phase diagram for type II superconductors. Below H_{c1} magnetic field is expelled from the superconductor. Above H_{c2} superconductivity is destroyed in the material, and between H_{c1} and H_{c2} is the mixed state in which the field penetrates as a regular array of vortices.

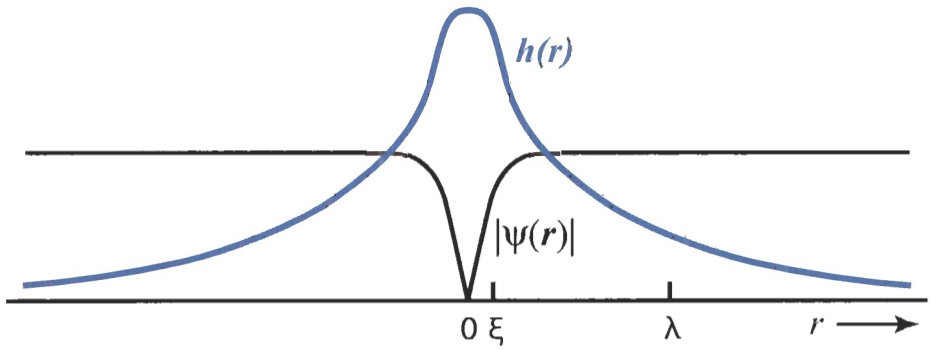

Figure 1.8: Magnetic field and superconducting wave-function profiles through the centre of an individual vortex, showing how they scales with the fundamental parameters ξ and λ.

The field profile of an individual vortex in the bulk of a superconductor is shown in Figure 1.8, adapted from ref. [29], where it is seen that the strongest field variation

occurs on a length scale $r = \lambda$ from the vortex core. Near the surface of the superconductor however, the flux spreads out further starting at a depth of approximately λ (see Figure ??) . The exact magnetic field profile inside and outside superconductor can be solved from London theory [15]. Pearl has modeled the field of a vortex above the surface to be like that of a magnetic monopole located beneath the surface a distance λ [25]. Since scanning Hall probe microscopy images the field just above the surface, this monopole model can be used to determine the penetration depth of a material from the image of a single vortex. The relevant penetration depth for the layered cuprates is the in-plane penetration depth λ_{ab}, and is related to the superfluid density, n_s/m^*, by the relation $4\pi\lambda^2/c^2 = m^*/n_s e^2$, where m^* is the effective mass of the quasiparticles, and n_s is the number density of superconducting electrons. The penetration depth is thus an important quantity to measure experimentally because it can give direct information on the superconducting state. For high-T_c superconductors in particular, measurements of the superfluid density are of great theoretical importance.

1.4.2 Scanning Hall probe studies of high T_c cuprates

The high temperature cuprates and scanning probe microscopy both have their beginnings in the 1980s at IBM research labs in Zürich, but it is somewhat of a coincidence that they ended up reconvening to produce theoretically important work in the cuprates in recent years. The discovery of superconductivity in LaBaCuO (LBCO) with a T_c of 35 K came in 1986 after a systematic study of various ceramic compounds by J. Goerg Bednorz and Karl Müller. Considered to be a giant leap in T_c relative to the previous 75 years' worth of research, their results were quickly verified by other groups around the world, only to be eclipsed less than a year later with the discovery of a related compound $YBa_2Cu_3O_{6+x}$, having an optimal T_c of 93 K, and making superconductivity available at liquid nitrogen temperatures. Since then, many other similar compounds have been found to be superconducting with critical temperatures up to 135 K. Although only about a factor of 2 away from room temperature, further advances in T_c have proven elusive and have prompted a barrage of

theoretical and experimental work involving many techniques including scanning Hall probe microscopy, to understand the underlying mechanism at work in these strange materials.

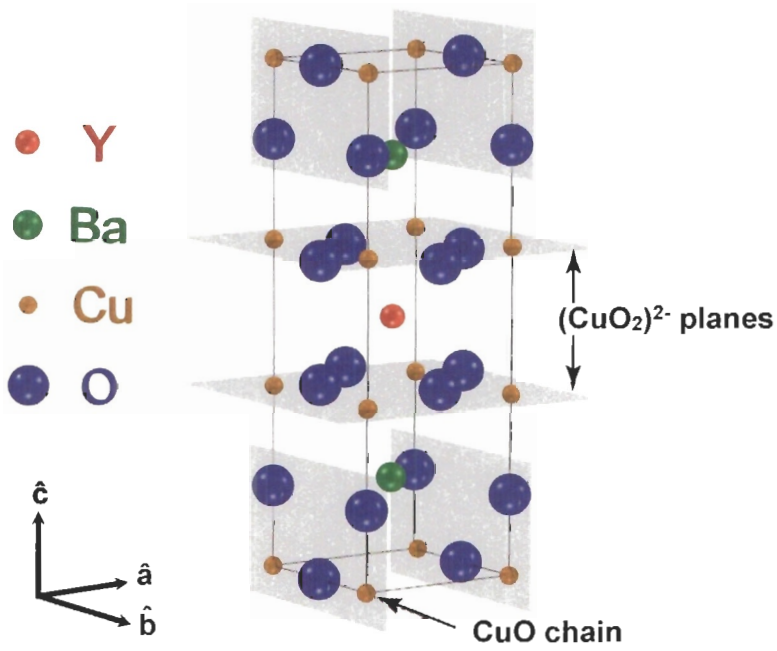

Figure 1.9: The unit cell for the high temperature superconductor $YBa_2Cu_3O_{6+x}$ (YBCO).

Unlike conventional superconductors, high T_c cuprates are highly anisotropic in their composition, with superconductivity occurring mainly in the copper oxygen planes. Figure 1.9 shows a representative unit cell for $YBa_2Cu_3O_{6+x}$ (YBCO). It has been established for some time that, in these materials, d-wave superconductivity arises with the addition of oxygen dopants to a parent Mott insulator compound. Furthermore the evolution of the physical properties from the insulator to the superconductor as a function of doping has been extensively studied in the last several years. As a consequence, the phase diagram sketched in Figure 1.10 has emerged for the cuprates. Agreement on the mechanism of superconductivity in the cuprates has not been reached, however.

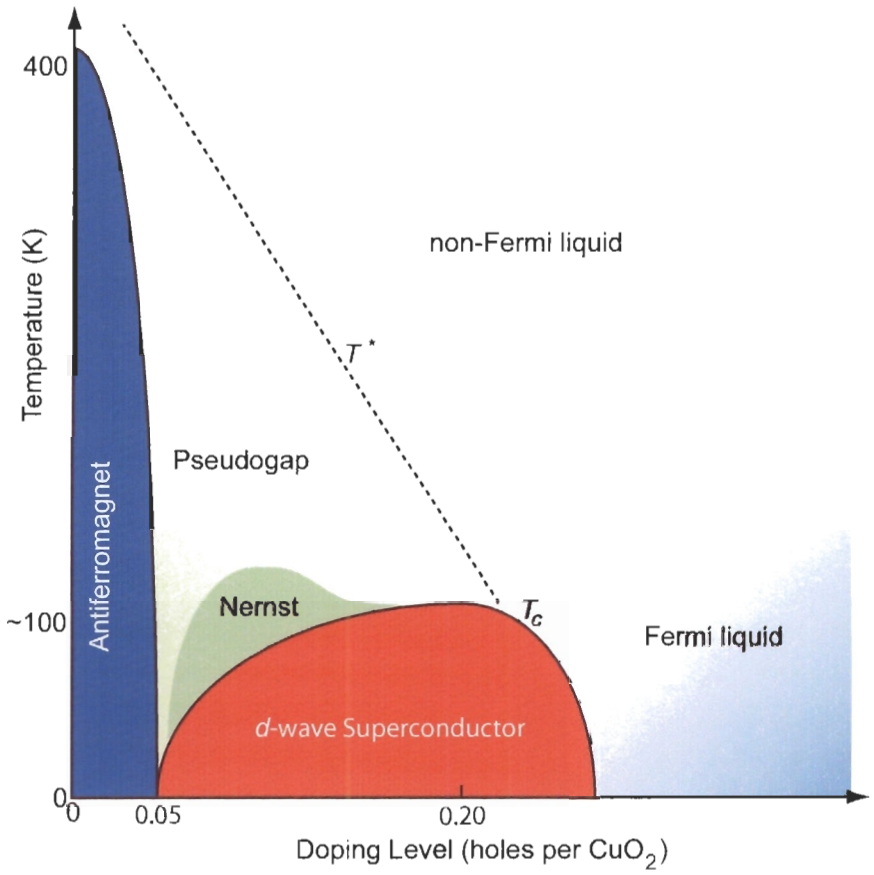

Figure 1.10: Idealized temperature-doping phase diagram of the cuprate superconductors. Courtesy of Wendell Huttema.

Some of the most elegant suggestions for the theory of high temperature superconductivity have come from implementations of Anderson's resonating valence bond model [30]. The most striking result to emerge is the prediction of spin-charge separation (SCS), in which the physical electron fractionalizes into a chargeless spin-half fermion (spinon) and a spin-zero charge-e boson (holon). A recent quantitative microscopic theory of SCS was formulated by Senthil and Fisher in 2000 [31], where they introduced an excitation called a *vison* that is accompanied by the existence of hc/e flux quantization in the underdoped cuprates. Advances in the preparation of heavily underdoped $YBa_2Cu_3O_{6+x}$ single crystals [32] made possible the testing of this theory by scanning SQUID and scanning Hall probe microscopy [26, 33] soon afterward.

In [26] Wynn et al. looked for the predicted hc/e fluxoids in $YBa_2Cu_3O_{6.35}$ samples with scanning SQUID and Hall probe microscopies. They imaged over 170 vortices, all of which carried the usual flux $\Phi_0 = hc/2e$. This set an upper limit on the vison energy that was much lower than that predicted by the theory. In case the lack of hc/e vortices was due to metastable $hc/2e$ vortices, they also performed an experiment proposed by Senthil and Fisher [34] that addressed the dynamics of visons and is thus a more stringent test of the theory. In this experiment, described in [33], they looked for a vortex memory effect in a 10 μm superconducting ring, the signature of a vison, only to again yield null results. Although there has been debate about the extent to which these experiments can settle the issue of SCS in the cuprates, Wynn writes that they deem unlikely at least one group of theories for the cuprates that predict visons and/or a vortex memory effect in the cuprates.

This was not the end of the story for SCS however, as Senthil and Lee have devised a new version of the experiment in which a pair of concentric superconducting rings must be fabricated on a non-superconducting background [35]. The inner ring has a critical temperature T_{c2} which is lower than that of the outer ring, T_{c1}, so that by first cooling the sample in a magnetic field to a temperature T_{in} such that $T_{c2} < T_{in} < T_{c1}$, the outer ring is used to trap an odd number of flux quanta in the inner normal region. In a spin-charge separated medium this must be accompanied by the presence of gauge flux.

Upon further cooling the sample just to get the inner ring to go superconducting, it will trap the odd flux quanta vortex. With the thickness of the inner ring being smaller than the physical penetration depth, most of the flux will escape; however, there will still be a small residual flux due to the current in the inner ring associated with the induced vortex. This residual magnetic flux can then be detected.

According to their theory, this effect only occurs if the initial vorticity in the outer ring is odd. If on the other hand it is even, there will be no induced physical flux when the inner ring goes superconducting and therefore nothing to detect. Our scanning hall probe microscope, when outfitted with a near-field optical probe for the persistent photodoping of single crystal $YBa_2Cu_3O_{6+x}$, will provide an excellent means of fabricating such a device and to perform this experiment. The key point is

that using this method, the material in between the rings can be highly underdoped, allowing the experiment to be carried out in the non-superconducting part of the phase diagram, beyond where the Moler group could access, and where SCS is more strongly expected on theoretical grounds.

Chapter 2

Sub-micron scanning Hall probes

Hall probes have flux sensitivity approaching that of SQUIDs and spatial resolution rivaling MFM; along with their quantitative, interpretable measurement and non-invasive nature, they possess all of the qualities to be the premier sensor for mesoscopic magnetic microscopy. There are still efforts to make smaller Hall probes, and unlike SQUIDs, they can in theory be arbitrarily small. However, to improve upon, or maintain the flux sensitivity, details in the electronic and thermal properties of the material used, as well as in the device geometry need to be considered. A thorough understanding of these issues is important for us, as Ricky Chu, a fellow masters student in our group, has started his research work on making sub-micron Hall probes using SFU's facilities for semiconductor growth, processing, and fabrication.

Following a brief review of the classical Hall effect, this chapter begins with a theoretical discussion of how the magnetic field sensitivity, and the fundamental limits on the size of small Hall sensors, depend on the properties of the material used. This is based on derivations carried out by David Broun. A section is then devoted to GaAs/AlGaAs Hall probes, as this material has been proven to possess excellent properties for Hall probe performance and has readily available fabrication technologies. As mentioned in the previous chapter, we have been given some state-of-the-art 150 nm GaAs/AlGaAs Hall probes by Clifford Hicks, a collaborator from Stanford University; these being the first devices to be used with our SHPM, their operating characteristics will be discussed here.

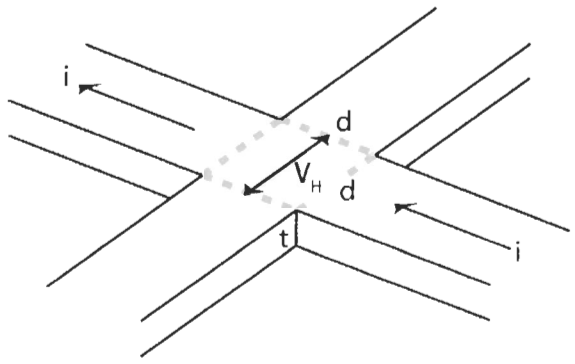

Figure 2.1: A Hall sensor consists a conducting cross of thickness t. A current is passed through one direction and, in the presence of a magnetic field that is normal to the dashed region, a voltage appears across the transverse direction.

2.1 The Hall effect

Hall probes rely on the simple principle of the Hall effect for their operation as magnetic sensors. Discovered by Hall in 1879, the Hall effect occurs when a current carrying conductor is exposed to a perpendicular magnetic field; the charge carriers are deflected in the transverse direction by the Lorentz force, and a voltage (the Hall voltage V_H) appears across this direction. This voltage is proportional to the current and field, and inversely proportional to the carrier density, n, of the conductor. The Hall effect is thus often used to determine n and the sign of the charge carriers in a material. However, it can also be used to quantitatively measure the magnetic field, the mode of usage that is of most importance to us.

To use the Hall effect for field detection, a conducting material is fabricated into a cross of thickness t, shown in Figure 2.1, and a current I is driven in one direction while the voltage V_H is measured across the other direction. The equation for the Hall effect in three dimensions is given by

$$V_H = \frac{IB_z}{n_{3D}te}, \tag{2.1}$$

where B_z is the average magnetic field penetrating the active region in the normal direction, and n_{3D} is the carrier density. Looking at this equation one can see that

by decreasing the charge density, the response of the Hall voltage to magnetic fields increases. For this reason Hall probes are often made from a two-dimensional conductor such as AlGaAs (described in Section 3.4) where the carrier density is very low. In 2D the thickness of the sensor drops out, and the Hall effect equation becomes

$$V_H = \frac{IB_z}{n_{2D}e} = R_H I B_z, \tag{2.2}$$

where $R_H = (n_{2D}e)^{-1}$ is defined as the Hall coefficent, which determines the response of the device to magnetic fields. Since small n leads to large R_H, and thus large field response, it is desirable to use a material with small n for a Hall probe. R_H for a device is normally found by calibrating the device in known magnetic fields.

2.2 Theoretical limits on Hall probes

2.2.1 Magnetic field sensitivity

Here I will show how fundamental properties of the material can be used to obtain a rather elegant form for the minimum detectable field of a Hall probe. Starting with the three dimensional Hall voltage,

$$V_H = \frac{IB}{nte}, \tag{2.3}$$

where the subscripts on the right hand side have been dropped, we can rearrange and substitute to find the minimum detectable field B_{min}.

$$\begin{aligned} B_{min} &= \frac{nte}{I} V_{min} \\ &= \frac{nte}{I} \sqrt{4k_B T R \Delta f}. \end{aligned} \tag{2.4}$$

Here we assume that the minimum detectable field corresponds to a signal-to-noise ratio of 1, and that we only have Johnson noise. In practice, however, this is not the only source of noise to contend with, because it is very likely that most semiconducting Hall sensors will show strong excess noise in the presence of a bias current, leading to $1/f$-like noise. This type of noise is discussed further in the following section.

In order to recast the expression for the minimum detectable field into a more transparent form it is useful to make the following definitions:

$$\begin{aligned} P_{th} &= 4k_B T\Delta f \qquad \text{the noise power at temperature } T \text{ in a bandwidth } \Delta f \\ P_{bias} &= I^2 R \qquad \text{the power dissipated in the active region by the bias current} \\ R &= \frac{\rho l}{A} = \frac{\rho}{t} = \frac{m^*}{ne^2\tau t} \qquad \text{the resistance of the active region} \end{aligned}$$

Where τ is the charge carrier life-time. Using these definitions to rewrite Equation (2.4), the minimum detectable field becomes

$$\begin{aligned} B_{min} &= nteR\sqrt{\frac{P_{th}}{P_{bias}}} \\ &= \frac{m^*}{e\tau}\sqrt{\frac{P_{th}}{P_{bias}}}. \end{aligned} \tag{2.5}$$

The effective mass is the ratio of the Fermi momentum to the Fermi velocity:

$$m^* = \frac{p_F}{v_F} = \frac{\hbar k_F}{v_F} = \frac{h}{\lambda_F v_F},$$

where λ_F is the Fermi wavelength. (Another useful relation involving the Fermi wavelength is that the electron density $n \approx 8/\lambda_F^3$, implying that the average spacing between charge carriers is $\lambda_F/2$.) Finally substituting the effective mass in terms of the Fermi wavelength and velocity, the minimum detectable field is

$$\begin{aligned} B_{min} &= \frac{h}{e\lambda_F v_F \tau}\sqrt{\frac{P_{th}}{P_{bias}}} \\ B_{min} &= \frac{\Phi_0}{\lambda_F \Lambda}\sqrt{\frac{P_{th}}{P_{bias}}} \end{aligned} \tag{2.6}$$

Here $\Phi_0 = \frac{h}{e}$ is the magnetic flux quantum for a *single* electron, and Λ is the mean free path of the charge carriers in the material. It will be shown below that the ratio P_{th}/P_{bias} can be as small as 10^{-12}, putting the Hall sensor into the realm of the SQUID for flux sensitivity. In fact, the expression for B_{min} closely resembles that of the SQUID, with the area of the SQUID loop replaced be the product $\lambda_F\Lambda$, which one should try to maximize subject to limitations placed by Hall-effect quenching and carrier density.

Sensor self heating – limits on the bias power

In the absence of excess noise, we can improve the sensitivity greatly by operating the sensor under a large current bias. In this case, the maximum bias current is set by how much sensor self-heating we can tolerate; however, in some cases, if the voltage drop across the active region associated with this bias current is large enough, it can cause charge leakage, effectively washing out the spatial definition of the Hall cross. We will assume that the temperature rise, ΔT, of the sensor above its surroundings is set by the thermal conductivity, κ, of the sensor material.

Taking this approach, the bias power is limited to

$$P_{bias} = \frac{\kappa A}{l}\Delta T.$$

The heat is being conducted through the active region into its substrate, so $A = d^2$ and $l = t$. We can relate the thermal and electrical conductivities of the material with the Wiedemann Franz law, and make the following substitions to get P_{bias} into a more useful form:

$$\begin{aligned}
\kappa &= \frac{\pi^2}{3}\frac{k_B^2 T}{e^2}\sigma \\
&= \frac{\pi^2}{3}\frac{k_B^2 T}{e^2}\frac{ne^2\tau}{m^*} \\
&= \frac{\pi^2}{3}k_B^2 T\frac{8}{\lambda_F^3}\frac{\lambda_F v_F \tau}{h} \\
&= \frac{8\pi^2}{3}k_B^2 T\frac{\Lambda}{h\lambda_F^2}
\end{aligned}$$

The bias power is then

$$P_{bias} = \frac{8\pi^2}{3}\frac{k_B^2 T\Delta T}{h}\frac{\Lambda d^2}{\lambda_F^2 t},$$

and so the ratio P_{th}/P_{bias} becomes

$$\begin{aligned}
\frac{P_{th}}{P_{bias}} &= \frac{3}{2\pi^2}\frac{h\Delta f}{k_B\Delta T}\frac{t\lambda_F^2}{\Lambda d^2} \\
&= 0.152\frac{h\Delta f}{k_B\Delta T}\frac{t\lambda_F^2}{\Lambda d^2}.
\end{aligned}$$

The minimum detectable field is

$$\begin{aligned} B_{min} &= \frac{\Phi_0}{\lambda_F \Lambda}\sqrt{\frac{P_{th}}{P_{bias}}} \\ &= 0.390\Phi_0 \frac{1}{\Lambda d}\sqrt{\frac{t}{\Lambda}}\sqrt{\frac{h\Delta f}{k_B \Delta T}}. \end{aligned} \tag{2.7}$$

To put this in perspective, a 1 K temperature rise corresponds to a frequency of 20 GHz, making the last factor 7×10^{-6} for a 1 Hz measurement bandwidth. For sensors fabricated from three dimensional metals, the electron mean free path is likely set by the thickness of the sensor, so the factor $\sqrt{t/\Lambda}$ will be of the order of unity. With these numbers, the minimum detectable field is

$$B_{min} \approx 2.8 \times 10^{-6}\frac{\Phi_0}{\Lambda d}.$$

The result is independent of λ_F — that is, it is independent of the electron concentration. This means that we are free to explore materials ranging from lightly doped semiconductors, through to heavily degenerate semiconductors and on to semi-metals and good metals like gold and aluminum. This gives us a lot of scope to address the problem of excess noise. The calculation above assumes that the heat will be transferred efficiently from the Hall sensor to the substrate, where it would have to be carried away by phonons. This may be overly optimistic in many cases depending on the substrate, but if the coupling to phonons becomes a problem we may want to turn to epitaxially grown semiconductor heterostructures where, because of their crystalline nature, there should be very efficient coupling of phonons through the various layers of the structure.

2.2.2 Fundamental limits on length scales

The material the Hall sensor is constructed from is described by two parameters, the Fermi wavelength λ_F and the mean free path Λ. The calculation in the preceding section suggests that the Hall sensor performance will be independent of λ_F (or electron concentration), leaving us to focus on optimizing the mean free path.

The width of the Hall sensor, d, places a fairly fundamental limit on how long the mean free path can be. If $\Lambda \ll d$ it is called the *diffusive* limit, in which each electron

makes multiple collisions within the active region of the Hall sensor. After each collision, the Lorentz force accelerates the electrons in the direction of the negative lead of the Hall device where some of them accumulate, building up a Hall voltage in proportion to the applied field. The disadvantage of this regime is when the carriers make too many collisions in the active region; the device then becomes very resistive, increasing the Johnson noise. Also in this limit, the current density extends partially into the voltage leads and approximately doubles the effective area of the probe. This makes for harder spatial interpretation of images when the magnetic field variations are on length scales smaller than the probe, and necessitates the computation of a response function for the Hall probe [15].

In the opposite limit, $d \ll \Lambda$, the electrons move *ballistically* through the active region, relatively free of collisions with other electrons. However, the electrons *can* make multiple collisions with the boundaries of the Hall junction before scattering from an impurity. For the most common Hall sensor geometries, where the corners of the Hall cross are rounded, the semiclassical electron trajectories are *chaotic* and they bounce around the active region like billiards. If the mean free path is long enough the chaotic bouncing has the effect of randomizing which lead the electron ends up in. The Hall voltage arises because there is a difference in the probability of an electron scattering into the left and right leads due to the Lorentz force; however, if the motion is sufficiently chaotic, the probabilities are equal and the Hall voltage is said to be quenched. To avoid Hall effect quenching while maximizing field sensitivity we require $\Lambda \sim d$. This scenario would also likely make the effective area of the Hall probe closer to its lithographic size instead of doubling it like in the diffusive limit[1].

2.3 GaAs/AlGaAs Hall probes

As mentioned above, fundamental properties of the material used for Hall probes strongly influence their performance. GaAs/AlGaAs has proven to be a very good semiconducting heterostructure because the two dimensional electron gas (2DEG),

[1] The website http://www.sp.phy.cam.ac.uk/SPWeb/research/qmch.html contains more information on Hall effect quenching.

onto which the Hall sensor is patterned, can have a low carrier concentration (large R_H), and high mobility μ for reasonably high conductance, reducing Johnson noise and allowing a high drive current. The term 2DEG refers to a thin sheet of conduction electrons that forms just beneath the surface of specially grown wafers. At low temperature, the electrons can have an extremely long mean free path, and long coherence times, making these systems ideal for studying coherent, ballistic transport through nano-scale devices. The ballistic limit in Hall probes, as discussed above, is undesirable; however the smallest GaAs/AlGaAs 2DEG Hall probes, at 100 nm, are approaching the mean free path of the electrons from above, putting these devices into the optimal regime where $\Lambda \sim d$.

2.3.1 Clifford Hicks' 100 nm-scale Hall probes

These heterostructures have been used for more than a decade to make low temperature sub-micron Hall probes with flux resolution of $1 \times 10^{-5}\ \Phi_0/\sqrt{\text{Hz}}$, comparable to the best scanning SQUID systems [8]. In recent years, some of the smallest GaAs/AlGaAs devices have been coming from the Moler research group at Stanford University [15], who encourage and are willing to assist other scientists who want to duplicate their probes. Clifford Hicks, a PhD candidate from the group, has given us three 150 nm Hall probes from his latest fabrication run in August 2005 to get us started [24]. The smallest functioning devices from this run were 100 nm, a step closer to reaching the spatial resolution of MFM.

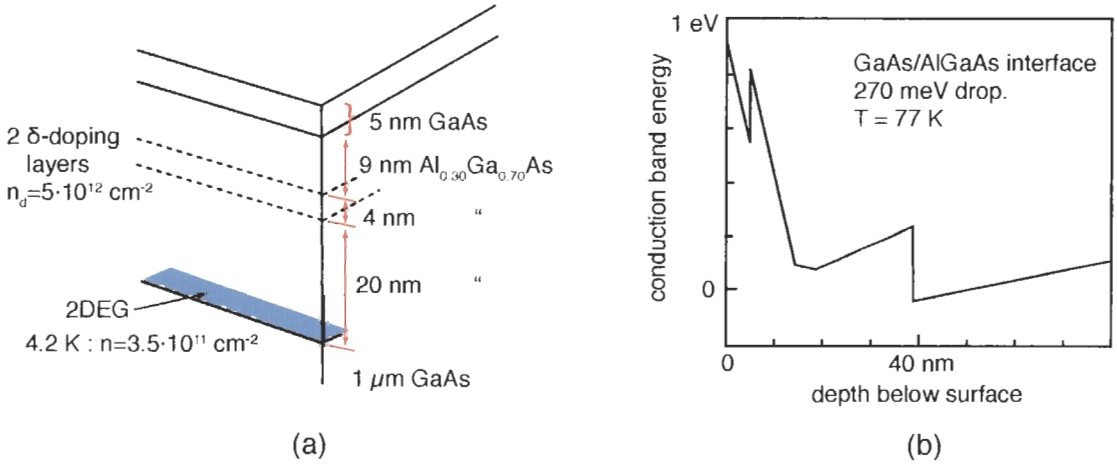

Figure 2.2: (a) A cross-section of the heterostructure grown by IQE Corporation showing the doping scheme that gives rise to a 2DEG 39 nm below the surface. (b) A plot showing the calculated conduction band energy as a function of the depth for the structure in (a) [24].

To obtain optimal spatial resolution in scanning magnetic microscopy it is not only necessary to have a small sensor, but the sensor must also be brought close to the sample. The ultimate lower limit on the height of the sensor for GaAs/AlGaAs Hall probes is the depth of the 2DEG, onto which the Hall cross is patterned — a shallow 2DEG is therefore essential. For the 150 nm Hall probes we have, Hicks used an extremely shallow 39 nm 2DEG in a δ-doped heterostructure grown by IQE corporation. A sketch and conduction band energy plot of the structure are shown in Figure 2.2. The structure has been doped such that at 4.2 K the unpatterned 2DEG has carrier density $n = 3.5 \cdot 10^{11}$ cm^{-2} and mobility $\mu = 2.5 \cdot 10^5$ cm^2/(V $\cdot$ s).

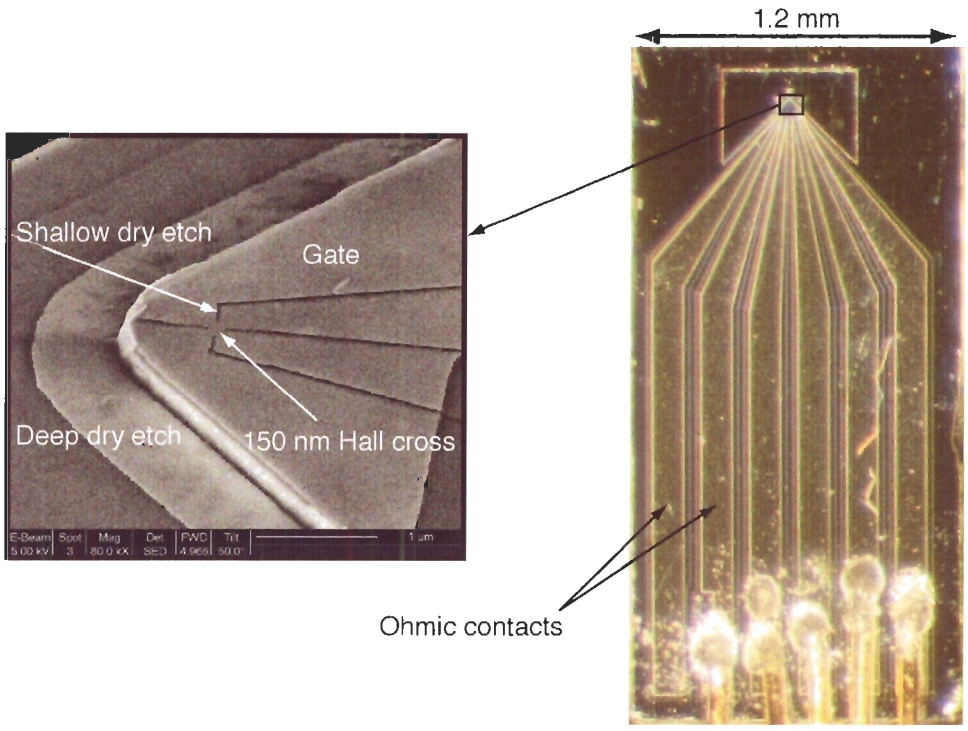

Figure 2.3: A picture of a 150 nm GaAs/AlGaAs Hall probe, fabricated by Clifford Hicks, taken through an optical microscope. There are six ohmic contacts on the device; the leftmost one is unused and is not connected to anything, the rightmost is for the gate electrode, and the middle four are the usual Hall sensor contacts. The wirebonding was done here in the lab using 100 μm gold wire, and Epotek H20E silver epoxy. The inset is an SEM image of one of these probes courtesy of Clifford Hicks [24].

A picture of one of our 150 nm Hall probes is shown in Figure 2.3. These probes were fabricated 20 to a wafer and then cut into individual probes. The first step in the fabrication process is the metallization for the ohmic contact pads which are 210 nm thick (Au, Ni, Ge). The thickness and constituents of the contacts are important to know when choosing a wire-bonding technique. After many attempts at gold wire-bonding with Bill Woods of Engineering at SFU, and another facility at UBC,

we ended up using silver epoxy (Epotek H20E) to bond 100 μm gold wires to the pads. Hicks suggested using aluminum wedge-bonding; however, no facilities for this technique were available at SFU or UBC.

An SEM image of one of these Hall probes is shown in the inset of Figure 2.3, indicating the subsequent fabrication steps [24]. The Hall cross itself is patterned by electron-beam lithography and reactive ion etching. This technique allows for the later deposition of a blanket gate for shielding from stray electric charges during scanning. The depth of the shallow dry etch defining the Hall cross is around 30 nm: enough to go through the dopant layers, but not through the 2DEG. It is sufficient however to cut off conduction in the 2DEG, and any deeper was found to increase the resistance through the device [4]. These trenches are also very narrow (20 nm) to facilitate the construction of the smallest possible functioning Hall probes. As a consequence, there is current leakage across the 20 nm lines at $\sim$100 mV at 4 K, and $\sim$10 mV at 77 K, so the operation of these probes is restricted to low temperature and moderate current.

When operating a foreign Hall probe, it is very useful to have some previous characterization of the devices to compare to. Thankfully, a thorough characterization has been reported in Hicks' 2006 APS March Meeting presentation [24] and in an unpublished paper of his [4]. The 2-point lead-lead resistance is any easy thing to check first, and then the Hall coefficient. At low temperature and zero gate bias, we have measured these to be around 18 kΩ, and 0.24 Ω/G respectively for the probe pictured above. The plots in Figure 2.4, from [24], show that the probe we were using was functioning as it should.

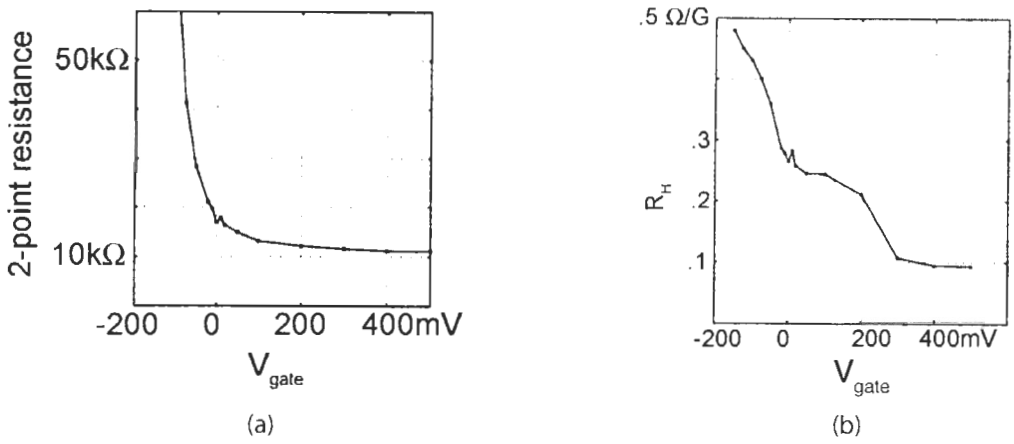

Figure 2.4: Plots from [24] showing the 2-point resistance (between two contact pads) as a function of gate voltage in (a), and the gate voltage versus Hall coefficient in (b), courtesy of Clifford Hicks.

Field sensitivity

Much work has been done to characterize the noise in small Hall probes because, as discussed in the previous section, it determines the minimum detectable field or sensitivity of the devices. The main sources of noise in Hall probes are Johnson noise, and excess noise ($1/f$ noise). The expected Johnson noise limit for these devices is $(4kTR)^{1/2}/IR_H \approx .05\text{G/Hz}^{1/2}$ at 77 K, where typical values for the 2-point resistance, drive current, and Hall resistance were used in the calculation [24].

Unfortunately the excess noise is the limiting factor on the sensitivity, and it comes in the form of random telegraph noise (RTN). RTN is a common phenomenon in small GaAs/AlGaAs devices, and can be seen clearly in the time traces of Figure 2.5 as discrete steps in the signal. It is strongly suspected that the RTN is caused by changes in the remote impurity or dopant configuration in the device, and that one impurity or donor hopping between two states constitutes a switcher at a single frequency. Telegraph noise from a single switcher is a Lorentzian in frequency space, but if the spectra of multiple independent switchers are added together the result resembles a

$1/f$ spectrum. $1/f$ noise can plague many larger devices, so continued research into RTN, which is likely the source of $1/f$ noise, could be of great importance not just to the operation of small Hall probes.

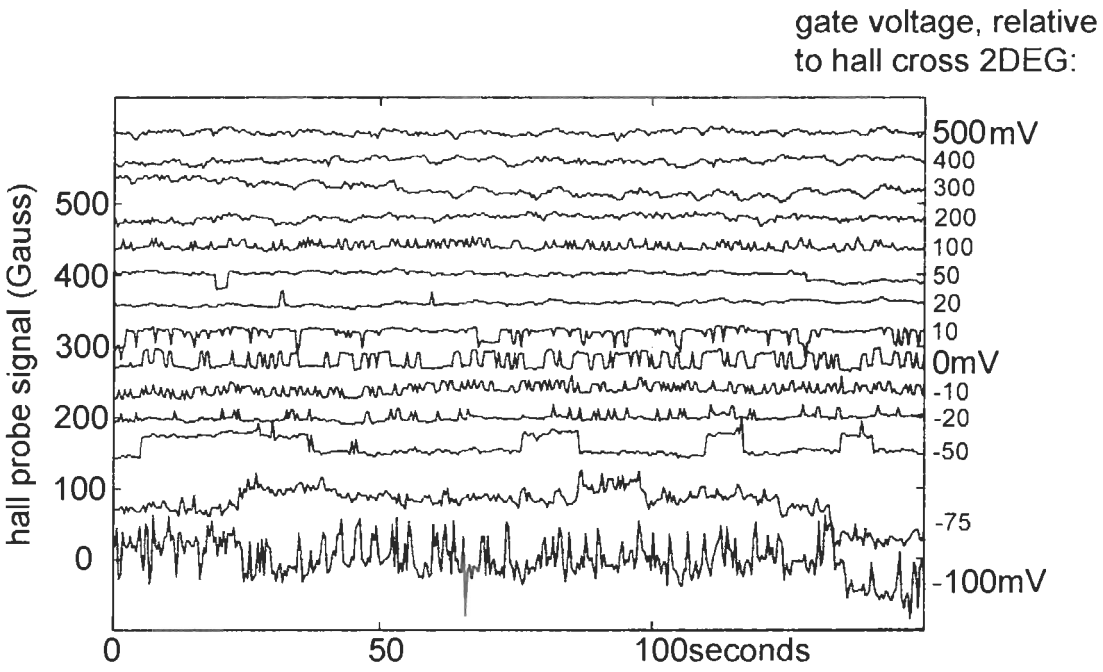

Figure 2.5: Plot from [24] showing time traces of the signal from a 150 nm Hall probe for various gate voltages. With around 20 mV between the gate and the Hall cross the random telegraph noise is nearly tuned out. Figure courtesy of Clifford Hicks.

Hicks has found that the amplitude of this excess noise grows rapidly for probes smaller than ~500 nm; thus minimizing it becomes essential if the devices are to continue to shrink. This is the subject of the study discussed in [4] where he systematically investigates how the sensitivities of 100 nm-scale Hall probes can be optimized by tuning the gate voltage and drive current. The largest switching events observed for 150 nm Hall probes were 9.6, 14, and 57 Ω, each for a different probe or cool-down, which for a Hall coefficient of $0.2\Omega/G$, would correspond to field noise of 48, 70, and 285 Gauss respectively. Time traces of the signal from a 150 nm Hall probe for various gate voltages are shown in Figure 2.5. Hicks found that tuning the gate is

more effective than tuning the drive current, and sensitivities of a few Gauss can be achieved for 100 nm-scale GaAs/AlGaAs Hall probes – good enough to image vortices in superconductors. Since imaging vortices will be the primary use for our SHPM, the 150 nm Hall probes we have are of great value to us, and they can be easily optimized for sensitivity on each cool down with our tunable gate voltage source.

Chapter 3

Mechanical design of the scanning Hall probe microscope

In the mechanical design of this scanning Hall probe microscope (SHPM), we have naturally drawn on concepts that are proven to be working in other systems. We felt however that some important components could be redesigned for our SHPM, and are therefore unique. A "double-gimbal" rotation stage for sensor angle adjustment, and a capacitive touch-down sensor incorporated into the sample stage are two examples. To aid in the complex design of the many components, and in the visualization of how they all fit together, the solid modeling software IronCAD was used extensively throughout the process. This allowed for slight modifications in the design to be made, and inspected in 3D, before machining any parts. In a physics experiment, mechanical design does not just involve the rendering of a drawing on the computer; the design has to work, and this involves calculations and careful material and adhesive choices. This chapter deals with the technical considerations associated with the key components of the mechanical design, and the characterizations thereof. But before launching into the details, I give an overview of the design and briefly discuss the functions of the various components involved.

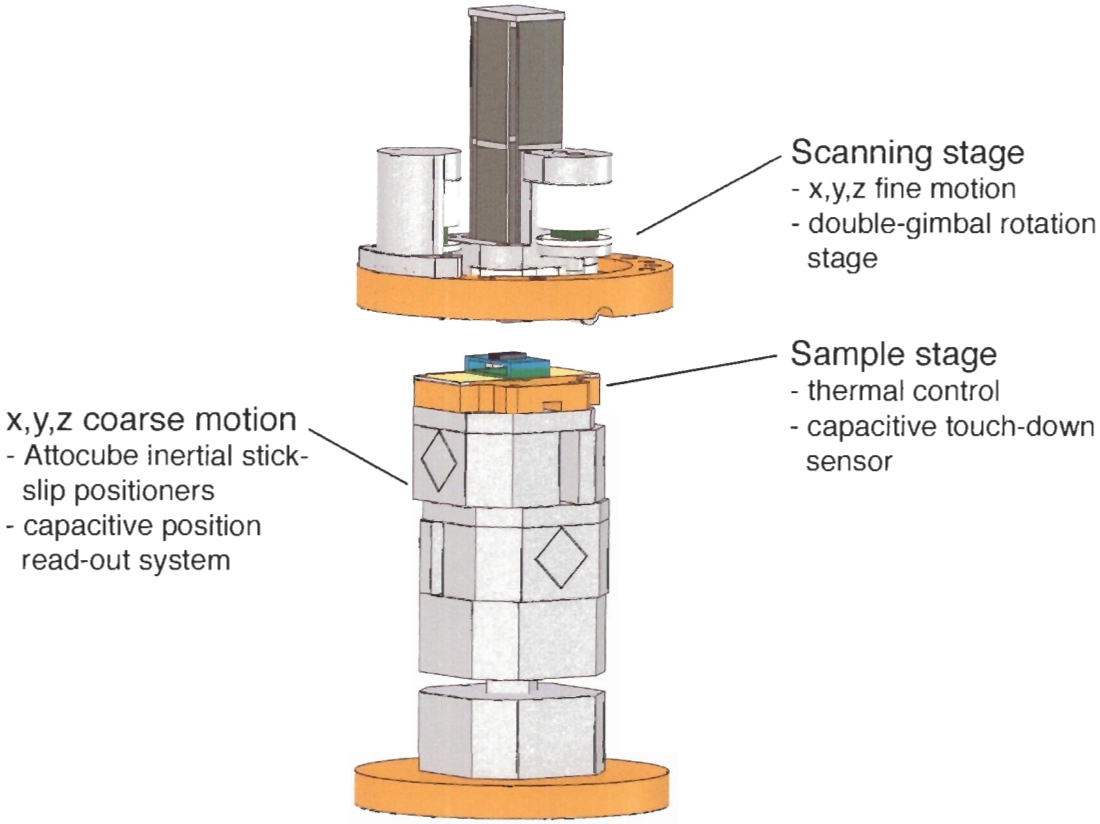

Figure 3.1: An IronCAD rendering of the SHPM showing an overview of the mechanical design.

3.1 Overview of the design

One of the design constraints that we had to work around from the beginning of the project was that the experiment be compact. This is important for a few reasons: one is that helium, the liquid used to bathe the experiment while in use, is expensive and therefore should be conserved if possible. By having a narrow helium dewar, and an experiment that fits neatly inside, one is making good use of the helium to cool the experiment, and not wasting it in void spaces. Another reason for a compact SHPM is that it must fit into a relatively narrow superconducting solenoid, as a homogeneous magnetic field is necessary to study vortices effectively. Finally we would like this experiment to be easily adapted to our dilution refrigerator, possibly as a "load-in"

experiment, necessitating a compact design.

In scanning Hall probe microscopy, it is desirable to have a large xy scan range so that one can image either many vortices in a single scan or larger magnetic features. The scanner should also be rigid to minimize vibrations and compact to fit into a small space as mentioned above. To meet this need we have used a design based on four piezoceramic S-benders that has been demonstrated to have a very large scan range at low temperatures [3].

To study high temperature superconductors with versatility, one must have very good control over the temperature of the sample. One must also make sure that the probe does not crash into the sample. These criteria have been taken into account in the design of an innovative sample thermal stage with a built-in capacitive sensor for touch-down detection.

When carrying out scanning probe microscopy, sample loading and sensor touch-down are done very carefully, so as not to destroy the probe or the sample. It is ideal to be able to pull the sample safely away from the probe when reloading or preparing, but also to be able touch down in a gentle yet rapid fashion. For this we have used commercially available Attocube positioners[1], which give us linear, inertial stick-slip x, y, z coarse motion of up to 7 mm per axis, and single steps down to a few nanometers. We have also addressed the need for an accurate absolute position read-out on these positioners by retrofitting them with variable coaxial capacitors designed by Taras Chouinard in our group. This could prove to be a powerful feature, enabling navigation between multiple samples in the same cool-down.

As discussed in the section on spatial resolution, it is important to be able to control the angle that the probe makes with the sample, to bring the sensing region of the probe as close as possible to the surface of the sample. For this we have come up with a novel double-gimbal design for the chassis of our scanner.

Another component that is crucial for placing vortices in a sample is a solenoid, which in our case is wound around the vacuum can. Previous studies show that a field of the order of one Gauss yields a density of vortices appropriate for SHPM [15], given

[1]We use the ANP 150x,y,z models, available from Attocube Systems, for our coarse motion.

the spatial resolution of the technique. This is useful information when designing our solenoid.

3.2 Sample stage with touch-down sensor

The sample stage sits on top of the coarse motion stage and gets positioned underneath the scanning stage with the Hall probe on it. For the sample stage we have come up with a unique design that combines thermal control and touch-down sensitivity for sensor approach and topography.

For this touch-down sensor, we needed to be able to detect small deflections caused by the sensor as it runs into the sample. To do this we used a parallel plate capacitor whose separation changes as the sensor touches the sample (see Figure 3.2). The sample platform with thermal control sits on the middle of a cover slip that is supported at its ends, on 200 μm spacers. It therefore is like a trampoline for the sample and with a 100 nm film of gold on the underside of it, it forms the upper electrode of the parallel plate capacitor. The other electrode is a solid brass disc embedded into the copper base of the sample stage. It has an area of 0.64 cm^2. We measure the capacitance of this configuration with an Andeen Hagerling capacitance bridge; by using the relation $|\Delta d/d_0| = |\Delta C/C_0|$ for small displacements, the deflection response of the sensor is 0.014pF/μm. Here d_0 is the equilibrium distance between the electrodes, and C_0 is the corresponding capacitance.

The sensitivity of the bridge allows us to detect deflections above a noise floor of $\sim$2 nm. Thus, we can detect very light touch-downs, which protects the sensor and the sample from damage and allows us to calibrate our z motion by compressing the trampoline over small distances. This also enables high resolution topographical imaging for calibrating our xy scanner. The touch-down sensor is most importantly a key component during scanning Hall probe imaging, where the sensor must ideally be scanned at a constant height above the surface of the sample. To do this, we perform touch-downs at multiple points over the intended scan range, then fit a surface to the resulting topograph. The sensor is then scanned over this surface, adjusted to be just above the sample. This is discussed in greater detail in the following section.

(a)

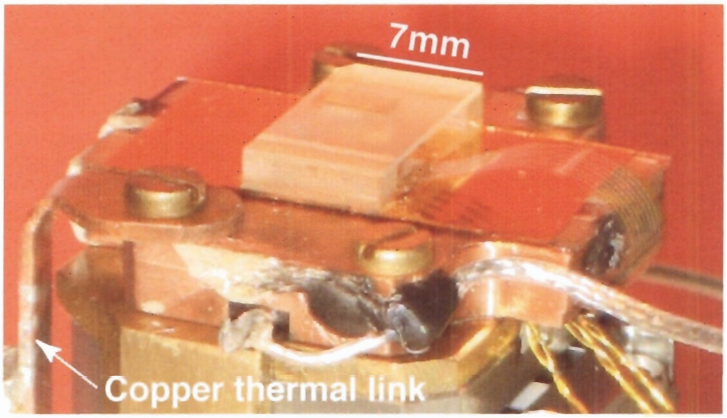

(b)

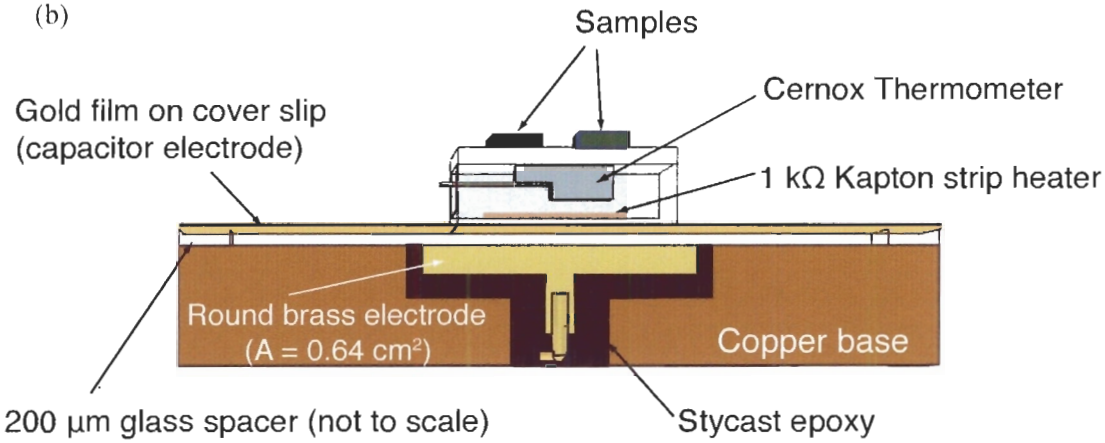

Figure 3.2: Sample thermal stage with capacitive touch-down sensor. Deflection sensitivity of ~2 nm is achieved using an Andeen Hagerling capacitance bridge for the sensor read-out.

3.3 Scanning stage

The scanning stage controls the fine motion of the Hall probe, as well as its angle with respect to the sample. The xyz piezo scanner is mounted on a chassis that has two axes of rotation (double gimbal) and can be taken in and out for easy repair or replacement. Here I discuss the details of the S-bender scanner and the double gimbal, and their characterization.

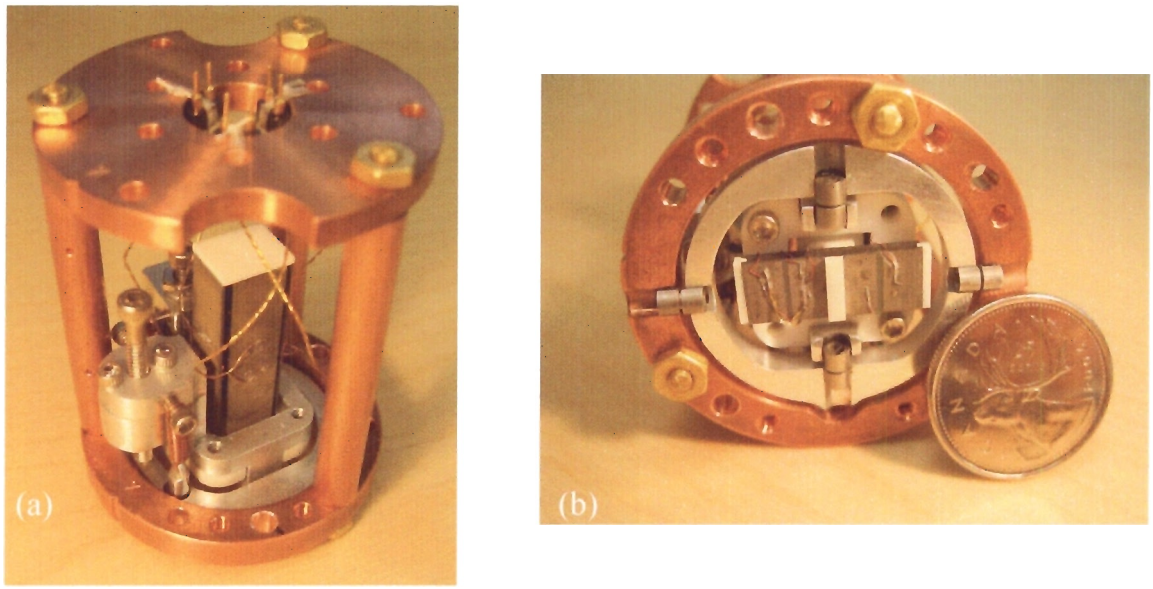

Figure 3.3: Pictures of the scanning stage. The gray strips seen in (a) are for the x, y fine motion scanner. The Hall probe gets mounted on the underside, pictured in (b).

3.3.1 Large area x, y scanner

Gerd Binnig, one of the winners of the Nobel prize for the invention of the STM, developed the piezoelectric tube scanner, which is well suited for small-range (less than one micron) and atomic resolution imaging. More recently, other scanning microscopy techniques have been developed such as scanning Hall probe microscopy, which measures spatial variations of magnetic field on a scale much larger than an atom. In that case, scan ranges of over 100 microns are sometimes desired. To address this need,

several approaches have been taken to design scanners with x, y ranges on the order of ten to a hundred microns. One is to simply use a longer piezo tube but, since scanning Hall probe microscopy has been adapted to low temperatures, where the piezoelectric response is reduced, this approach would require a tube that is too long and floppy for practical purposes. The answer lies in an alternative design first demonstrated by Siegel and coworkers in 1995 that uses a configuration of piezo S-benders and Macor (a machinable ceramic), to create a compact, large range cryogenic scanner [3]. With 2.5 inch long benders, a low temperature scan range of 270 μm was achieved; this is much greater than that of the largest tube scanner at the time with a range of only 9 μm. This design is superior to the piezo tube scanner in terms of its translational response, rigidity, and thermally compensated configuration; it is therefore particularly successful in meeting our criteria, and has been adopted by the Moler research group at Stanford for their scanning Hall probe microscope to produce reliable images of vortices.

Our scanner is constructed of segmented PZT piezoceramic bimorph benders (S-benders)[2], and Macor, see Figure 3.4(a). These materials are well matched in terms of their thermal expansions, and thus can be bonded together with cyanoacrylate (Superglue) without cracking during thermal cycling. Although the construction is fairly complex, it can be made precise with proper design and careful machining of the Macor pieces. The use of a jig during the assembly of the scanner with Superglue ensures this precision and makes for a robust structure. The electrodes on the benders must be segmented and wired in the particular way shown in Figure 3.4(b), so that when a voltage is applied across the opposite pairs of electrodes, the lower half of the bender curves in one direction while the other half curves in the opposite direction. This way, both ends of each bender remain at all times perpendicular to the direction of motion, as required by the boundary conditions imposed by the Macor pieces to which they are glued. Unsegmented benders curve in a "C" shape, and a scanner built with these would not work. Independent x, y motion of the scanning head, to which the fine z motion and probe are mounted, is achieved by applying equal bipolar

[2]The piezo bimorph material was purchased from Piezo Systems, Inc.

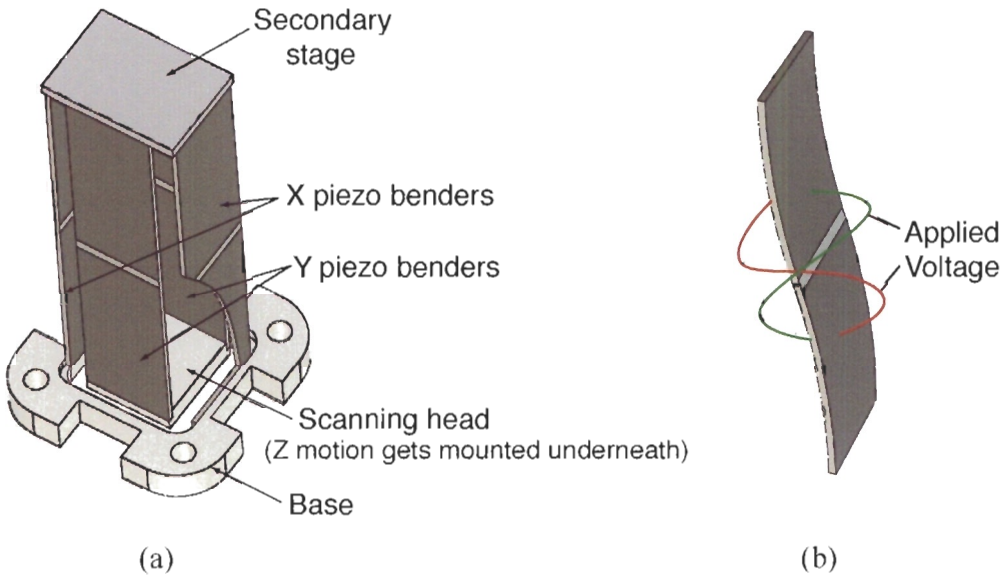

Figure 3.4: The scanner is made of a configuration of segmented piezoceramic benders and Macor pieces (a). When voltage is applied, the benders take on the "S" shape shown in (b). This design is based on one originally demonstrated by Siegel et al. in 1995 [3] and has since been used by various groups for scanning Hall probe microscopy.

voltages to the x or y pairs of benders. Having the two identical pairs of benders configured in this way also leads to thermal compensation of the scanning head; when the scanner is cooling, the x and y pairs contract by the same amount, leaving the probe height unchanged.

The high performance PZT bimorph material came in sheets $1.25 \times 2.5 \times 0.019$ inches thick. Being bimorphs, they consist of two layers of oppositely poled PZT ceramic separated by a centre brass shim. For electrodes, they have a thin nickel coating on each face, and when voltage is applied across them, an electric field is set up through the layers such that one layer of PZT contracts, while the other expands causing the whole thing to bend. To build a short range (1.25 inch long benders), and a long range scanner, the sheets first needed to be precisely cut into strips 0.3 inches wide using a wire saw. The electrodes were then segmented and wired. The segmentation was done by coating all but a 1 mm strip across the middle of the nickel

electrode with conformal coating[3], which is a clear enamel that masks the nickel from being etched. This strip was then etched with a 20% Nitric acid solution, taking about 10 minutes for the two new electrodes on each face to become electrically isolated. They were then wired as shown in Figure 3.4(b) under a microscope using small dots of solid core solder, and flux to contact the nickel surface.

The governing equation for the deflection of an S-bender is given by

$$x = d_{31} V \frac{L^2}{T^2}, \tag{3.1}$$

[3], and it is easy to show why it is half the response of an unsegemented bender. Here V is the applied voltage, L is the length of the bender, T its thickness, and d_{31} the piezoelectric constant (strain per applied electric field). It was demonstrated in [3] that the low-temperature (4.2 K) response is decreased by a factor of 8 from room temperature. This was verified during an earlier dip-probe experiment we carried out, where we characterized the response of a bender at 300 K, 77 K, and 4.2 K. One thing that is not discussed in [3] however, is the increase in the depolarization field of the material at low temperatures. As seen in the above equation, the maximum deflection is limited by the length of the bender and the maximum applied voltage, which depends on the depolarization field. With an increased depolarization field you can drive the benders harder, and achieve the same scan range with a shorter bender. We showed that the benders could be driven to about 600 V before the response became hysteretic and non-reproducible, meaning that the bender was irreversibly damaged. This is twice the voltage applied in [3], where the discussion focuses on comparing the response and resonance of a tube scanner with the double S-bender design. The S-benders win out in both categories. Siegel's design was not, however, fully optimized for a high resonant frequency. The lengths of the benders come into the resonant frequency as $1/L^2$, so by applying twice the voltage, the lengths of the benders can be reduced by $1/\sqrt{2}$, for the same range, thereby increasing the resonant frequency by a factor of 2.

Calibration of our 2.5 inch long scanner showed it to have a room temperature response of 3.3 μm/V, and a 4.2 K response of 0.43 μm/V, implying a low temperature

[3]Conformal coating is made by M.G. Chemicals.

600 V scan range of 520 μm; almost double the range demonstrated in [3]. This sort of range exceeds what would normally be needed for most practical scans, but should find some good applications, possibly in the writing of superconducting devices with the near-field scanning optical probe. Since our method of calibrating the x, y motion depends on the calibration of the z motion, discussion of x, y calibration is deferred until later in the chapter.

Self-resonance in the scanner becomes a factor when scans need to be taken quickly. Moreover, as probe sizes continue to shrink, small vibrations in the probe can compromise spatial resolution. A stiff scanner is not as susceptible to these vibrations and allows for faster scanning, so a scanner should be optimized to have a high resonant frequency. Cited in [3] is the resonant frequency of the x and y pairs of benders:

$$f_0 = 0.262 \frac{T}{L^2} \sqrt{\frac{Y_{11}}{\rho}}, \tag{3.2}$$

where Y_{11} is the bulk modulus of the material, and ρ its density. By comparison, in terms of translational sensitivity $s = x/V$, the resonant frequency of a tube is $f_0 = 0.0895 d_{31} \sqrt{Y_{11}/\rho}/(sT)$, whereas it is $f_0 = 0.262 d_{31} \sqrt{Y_{11}/\rho}/(sT)$ for the benders; nearly three times higher. So clearly the configuration of S-benders, although more difficult to construct, is better for our purposes. The actual resonant frequencies of the pairs in the scanner get lowered however, due to the additional mass of the Macor pieces and fine z motion. Using an optical interferometer, Siegel et al. have measured the amplitude response of the scanner to a small sinusoidal voltage to determine the room temperature resonances in the x and y directions. They were at 45 Hz and 73 Hz respectively; the y resonance being lower since the x benders carry the additional mass of the y benders and the secondary Macor stage. Using the stiffness of the PZT bimorph material given in the data sheet, I calculated the resonances of our scanner to be roughly the same. Although fairly low, the steps the scanner takes during a raster scan are at most 10 Hz, well clear of these modes.

3.3.2 Fine z motion

To design a long-range fine z positioner we employed the same set of principles as the x, y motion and used segmented benders. We use two benders that are segmented twice, one quarter of the way in on each side. In this way, they bend with a hump in the middle, while the ends stay horizontal and parallel. By spacing the ends of these benders with Macor pieces and driving them with opposite polarity, we were able to get a range of around 14 μm at 4.2 K. One bender gets fixed to the scanning head in the middle with Superglue, and a Macor platform is glued to the middle of the other bender where the sensor gets mounted.

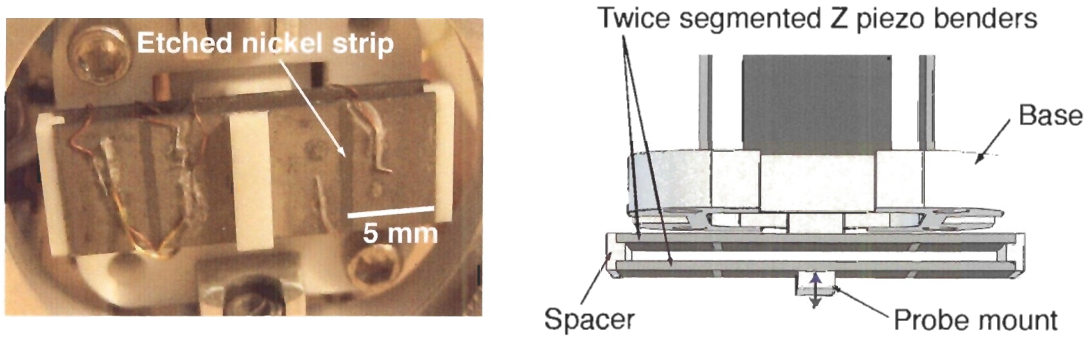

Figure 3.5: We have used two twice segmented piezo benders spaced apart at the ends to achieve $\pm$ 7 μm of z motion for the probe.

3.3.3 Fine motion calibration

For the calibration of the scanner we use the capacitive "trampoline" sensor described earlier. Recall that the room temperature response of the touch-down sensor is 0.014 pF/μm, and it can measure displacements down to $\sim$ 2 nm. The z motion is calibrated first by simply compressing the touch-down sensor; then for the lateral motion, we use an STM tip touch down at series of points over a grating, and use the

resulting topograph for calibration. A schematic of the set-up used for topography and calibration is shown in Figure 3.6.

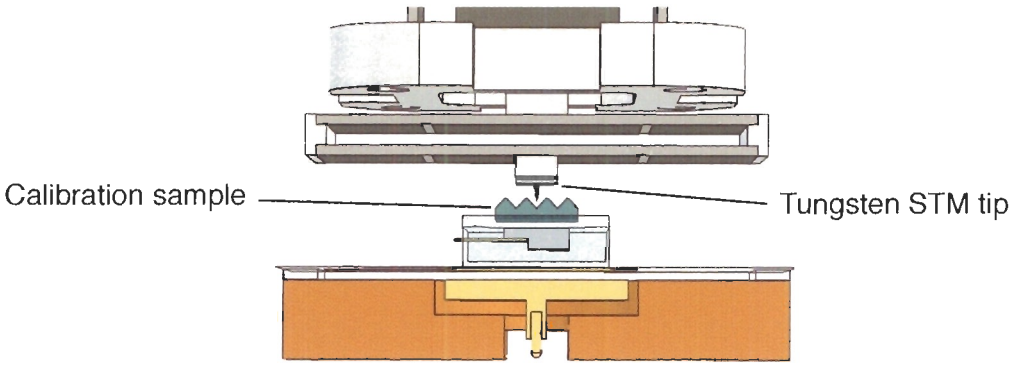

Figure 3.6: A schematic showing the set-up we use for topography and calibration of the scanner. Everything is to scale except for the grating shown on the sample stage.

z calibration

Because the cover slip used for the upper electrode is flexible, it takes little force to compress, making it ideal to calibrate our z motion over small distances. Calibration of the z motion must be done first because the topography technique we use for lateral calibration relies upon it. To do this we mounted a tungsten STM tip where the Hall probe is meant to go, and then gently stepped it into and out of the sensor over less than a micron while recording the capacitance. Figure 3.7 shows the data from this procedure. The flat part on the bottom left is from when the tip had not yet reached the sample stage. The inclined section is from the tip compressing and decompressing the trampoline a couple of times. Since points are all lying on top of each other, we can say that there is very little hysteresis associated with this motion. The slope of this line gives a response of 11 nm/V for the z motion. The D/A card we use from National instruments (PCI-6703) has 16 bit resolution, meaning that with the amplifier set at a gain of 10, we should still have sub-angstrom precision on our z

motion, however; precision on the order of nanometers is fine for our purposes.

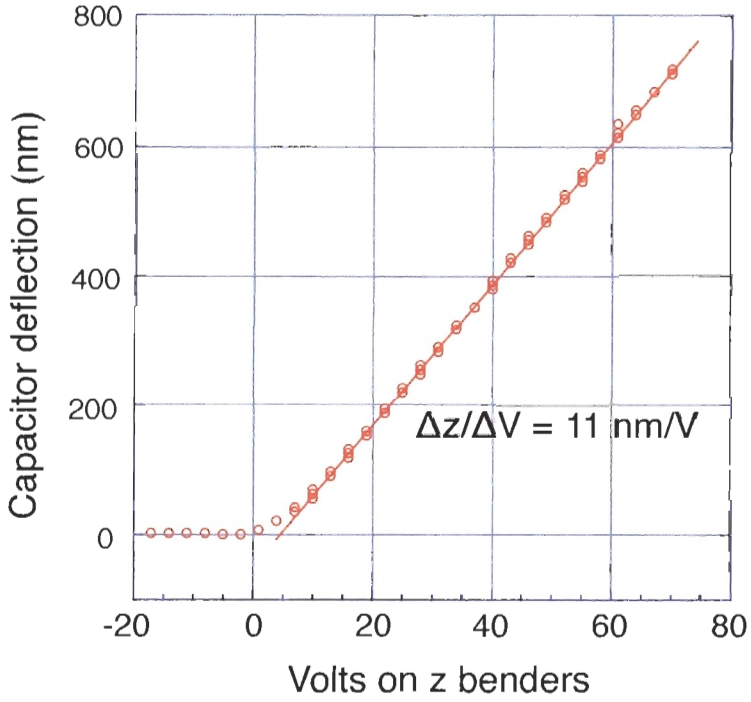

Figure 3.7: A plot showing the calibration of the z motion at 4.2 K

x, y calibration

For the lateral (x, y) calibration of the scanner we use the calibrated z motion combined with the capacitive touch-down sensor to obtain the surface topography of a silicon calibration grating[4] shown in Figure 3.9(b). First we stick the sample down to the capacitive stage with GE varnish so that the grid lines are oriented perpendicular to the x or y direction of the scanner wishing to be calibrated. In this way, a single line topograph of the grating is sufficient to calibrate either direction of the motion. To obtain the topograph, we wrote a LabVIEW script to do a series of touch-downs with the STM tip along a line or for a grid of points. At each point, the tip starts

[4]The calibration grating we use is an Ultrasharp TGF11 borrowed from John Bechhoeffer. They are available from MikroMasch Inc., www.spmtips.com.

from about 1 μm above the surface of the sample, then steps towards it in increments of $\sim$0.2 μm, between which the capacitance is checked, until it changes enough to indicate a light touch-down. The tip is then retracted and moves to the adjacent point for another touch-down and so on. For each x, y point on the grid or line, the z position of the tip upon touch-down subtracted by the small deflection of the capacitor, when plotted, gives an inverted topograph of the surface of the sample. Multiplying by negative one gives the actual surface topography.

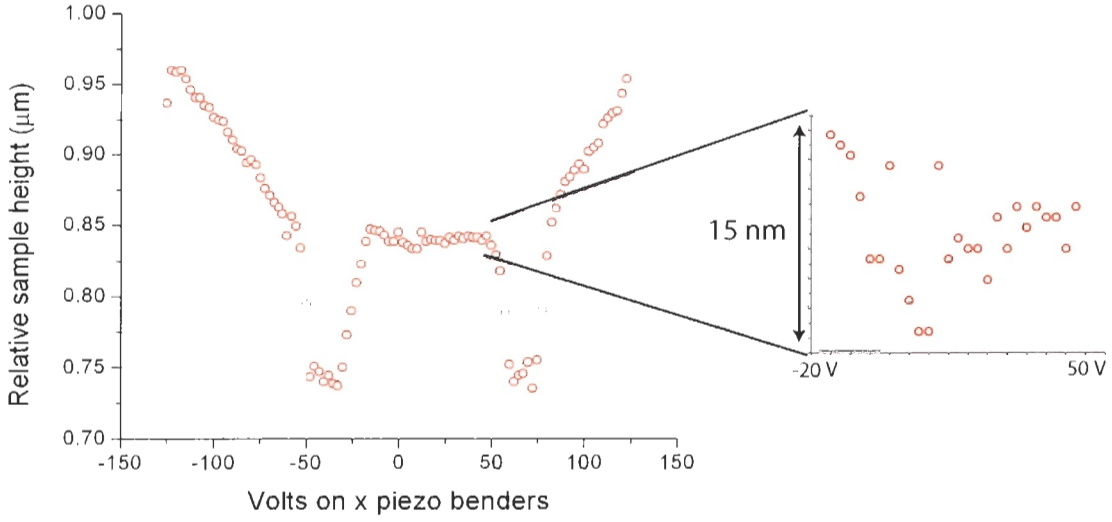

Figure 3.8: The first calibration attempt of our short range scanner. This is a line topograph in the x direction on a sample provided by Saeid Kamal. It was a test piece from a cleanroom course where he used photolithography to define 100 nm thick features on silicon. The sample was oriented here such that a set of 100 μm spaced lines were oriented perpendicular to the scan direction. With our short range scanner we could only pick up one of these lines, but the plot demonstrates the height sensitivity of the technique and could be used to crudely calibrate the x motion using only one duty cycle of this "grating".

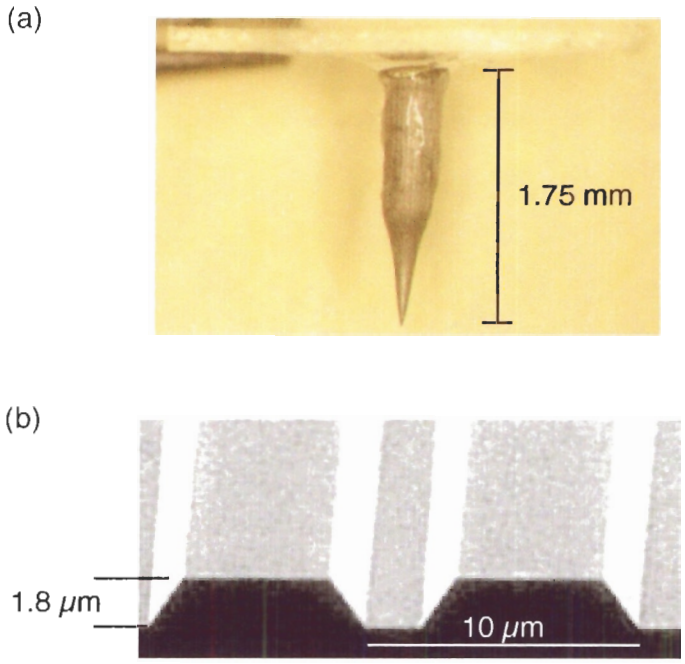

Figure 3.9: The tools used for calibration of the scanner. (a) A tungsten STM tip made using John Beehhoefer's facilities. Tungsten is good because it is strong and does not deform easily during touch-downs. (b) SEM image of the TGF11 silicon calibration grating we use for lateral calibration.

In a first attempt of using topography for calibration at room temperature we used a piece of silicon patterned by Saeid Kamal during a clean room class. He informed me that the thickness of the patterned structures was 100 nm. Figure 3.8 shows a line topograph taken perpendicular to a pattern of 50 μm stripes on the sample. This demonstrates the height sensitivity of the technique, which is very important in scanning. The step in the middle comes out to be about 100 nm tall, and the inset shows the plateau region to have a scatter of < 15 nm. Since we have only one full duty cycle of the pattern in our scan range, the sample is not ideal for lateral calibration.

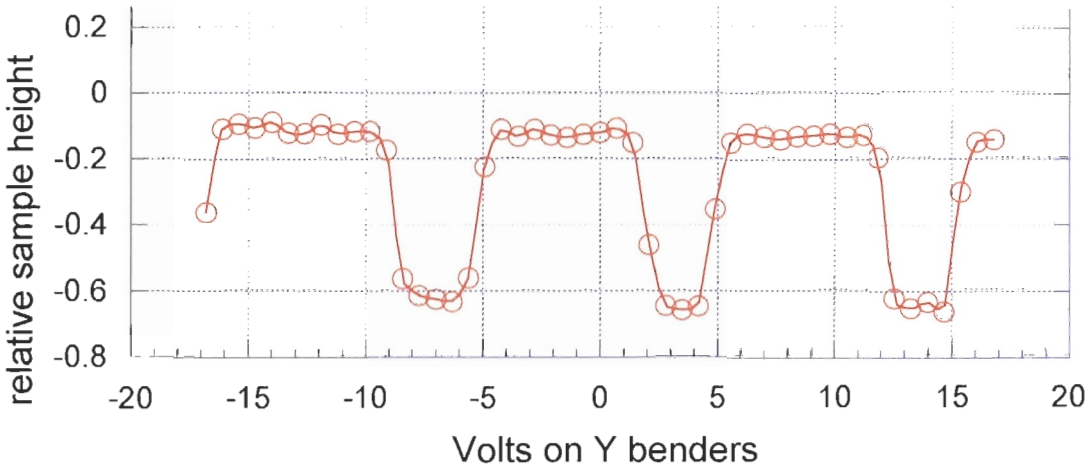

Figure 3.10: A room temperature topographic line-scan in the y direction of the TGF11 calibration grating illustrating the technique used for lateral calibration of the scanner.

Figure 3.10 shows a single line topograph in the y direction of the TGF11 grating taken at room temperature with our short (1.25 in.) scanner. It is one of the first and the best line-scans I took, demonstrating the capability of this technique using this grating, as well as indicating that this scanner was working in the y direction by the uniformity of the profile. This plot resembles well the profile seen in the SEM image of the TGF11 grating, and even the nominal surface roughness is seen as slight variations in height on the plateau regions. Most importantly for calibration purposes, the pitch of the grating is clearly visible; however, the troughs are not 1.8 μm deep as they should be according to the spec sheet. This is likely due to the tip not being sharp enough to get down to the bottoms of them. Larger scans make for better analysis and calibration of the motion, however from this scan the y response can be calculated to be $\sim$1 μm/V by taking the voltage spacing from the three duty-cycles in the the profile, which occur over 30 μm. At low temperature, the response is decreased by a factor of 8 and thus becomes ~ 0.13 μm/V.

Shortly after this topograph was taken, I accidentally crashed the tip into the grating, deforming the tip enough to compromise the nice lateral resolution seen in Figure 3.10. This was not the only set-back however. With a new tip mounted, the

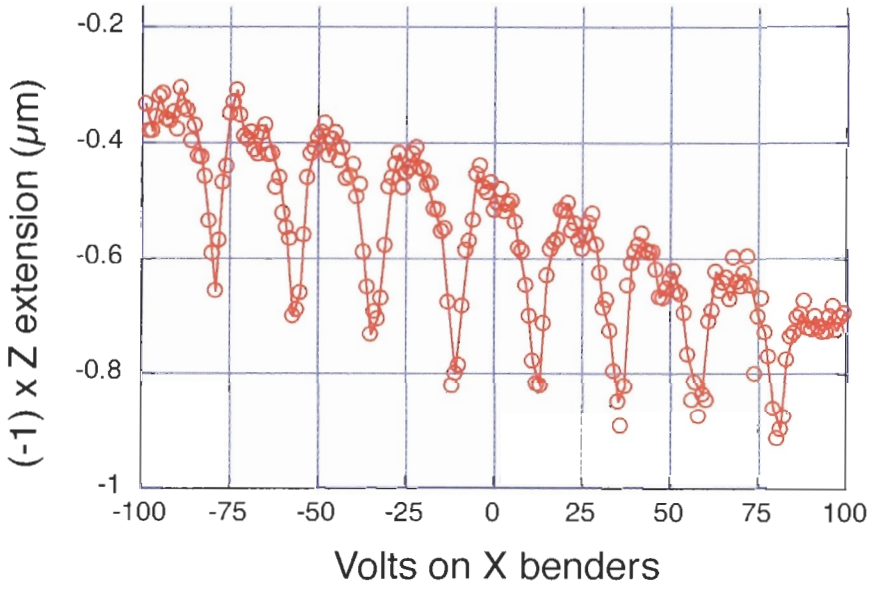

Figure 3.11: A topographic line-scan in the x direction of the TGF11 calibration grating taken at 4.2 K. From this data the response of the pair of x benders is determined to be 0.44 μm/V.

scanner was cooled down for an all-important low-temperature, long range calibration; but in the process, with about 550 V on the benders, we believe there to have been arcing across the electrodes that produced a burst of heat, boiling off about a liter of helium in a matter of seconds. After things had settled down, repeated attempts were made to detect the touch-down of the tip, but with no success. Upon warming up the experiment and inspecting it, I discovered that the piezo scanner had come apart at multiple glue joints, and there was evidence of oxidation on some materials. Extreme heat is not good for the piezo elements as they have a Curie temperature of 190 C, above which they may be irreversibly damaged due to depolarization, so a new scanner needed to be built. This ordeal set us back but, on the bright side, it *did* give us a new upper limit on the voltage to apply to the benders.

Using the procedures discussed earlier in this section, I constructed and calibrated a new scanner, this time, however, with piezo benders twice as long. The 2.5 inch long benders had already been segmented, with the intention of building a very large range

scanner, and were thus readily available for building a new scanner. The drawback in using benders twice as long, is a reduction by $1/4f_0$ in the resonant frequency of the scanner. A future student will build another shorter range scanner to address this concern.

The data from a low temperature calibration of this 2.5 inch scanner in the x direction is shown in Figure 3.11. Although this topograph is not as nice looking as the one from Figure 3.10, the periodicity of the grating is still apparent and was used to determine the response of the x pair of benders to be 0.44 μm/V. Using the 16 bit voltage resolution available from the D/A card, then dividing by the amplifier gain of 30 (the low-temperature setting for large-range scans), a minimum step size of less than a nanometer should be possible with this scanner. Not only can it take small steps at low-temperature, the long benders allow for a large-range. If we say the maximum voltage we can apply without risk of arcing is 500 V, then this scanner has a maximum range of 440 μm. This is a very large range relative to other scanners, but if even larger images wish to be taken, we can use the coarse motion to access adjacent scan areas and then stitch the images together.

Topographic imaging is not only used for calibration of the scanner but, of equal importance, it is used to determine the surface over which the sensor will be scanned during magnetic imaging. The details of this surface fitting procedure will be discussed in a following section.

3.3.4 Double-gimbal angular positioner

(a)

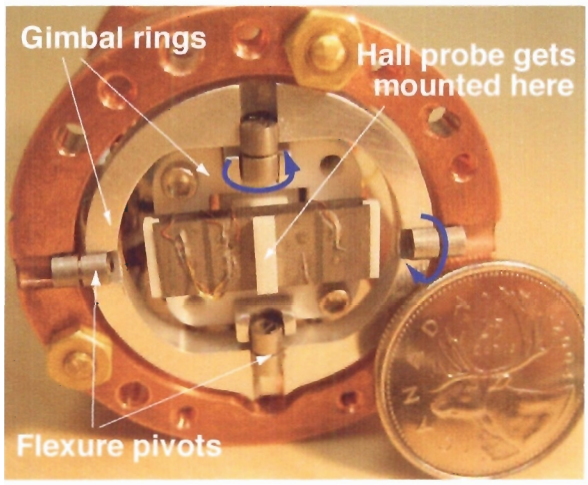

(b)

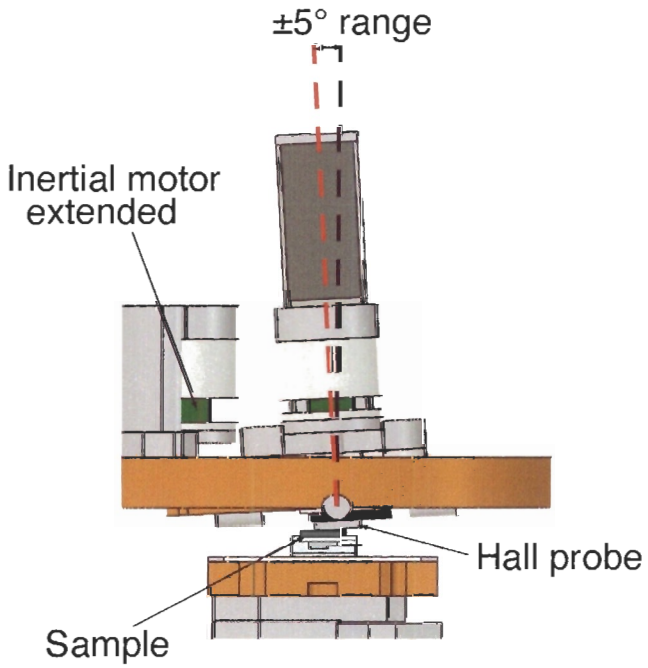

Figure 3.12: The probe angle adjustment is made possible by having the scanner mounted on an arrangement of three rings held together with flexure pivots, known as a double-gimbal. The hall probe sits on the probe mount which is on the innermost ring shown in (a). Adjustments are made by pushing or "pulling" on the rings using a spring loaded set screw. The drawing in (b) shows this to be done with miniature inertial stick-slip motors from Attocube; something that is planned for the near future.

As mentioned in the section on spatial resolution in the introductory chapter, the alignment of the Hall probe chip with the sample is very important to optimize spatial resolution in the SHPM. The Hall probe chip must be adjusted so that the active region of the probe, which detects the magnetic field, is as close as possible to the surface of the sample. The way this is commonly done in other groups is to introduce a small angle of 1-2° between the sample and the Hall probe at room temperature, by putting the sample on an angle adjustable stage. This method has had success in producing good images, however it does not leave the option of fine tuning the angle *in situ* to obtain optimal resolution.

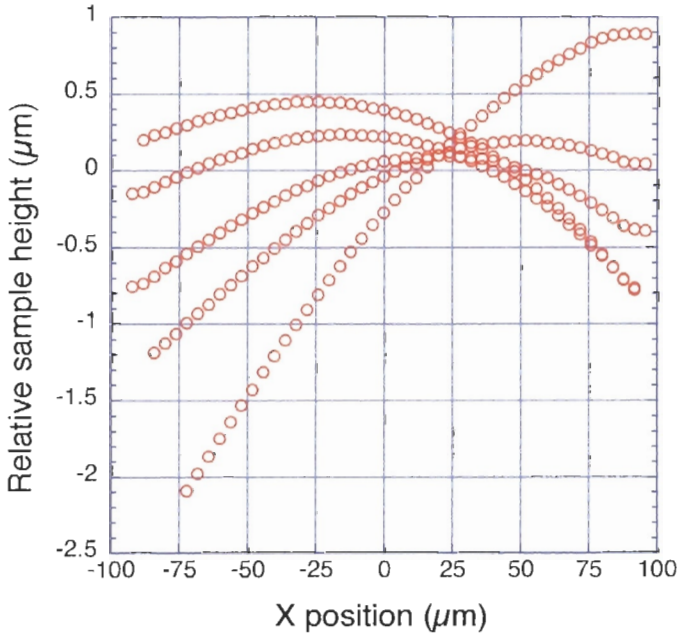

Figure 3.13: Each trajectory of points represents a line topograph in the x direction of a clean sapphire sample. The angle of the scan plane was adjusted by about 1/4 turn of the set screw on one gimbal axis between each line-scan.

Rather than mounting our sample on a rotation stage, we have incorporated the angle adjustment into our scanning stage by mounting the scanner on the inner ring of a two-axis gimbal chassis, borrowing from aerospace navigation and shipboard technology. In this way, the angle of the probe relative the sample can be adjusted as

seen in Figure 3.12(b), and eventually controlled in situ using miniature inertial stick-slip Attocube positioners. These have 3.5 mm of travel, giving us an angular range of 10 degrees for each axis, which is more than enough. The 1-2° will be introduced at room temperature and then fine adjustments will be made with these positioners at low temperature to get the sensor parallel to the sample for optimal resolution.

While we wait for the opportunity to buy or make these miniature positioners, we use the brackets designed to take the Attocubes, but with spring loaded set screws threaded through them instead. It is easy to fine tune the angle of the probe relative to the sample with the aid of an optical microscope, while turning these set screws. Figure 3.13 shows various line topographs on clean sapphire, taken one after the other with ~1/4 turn angle adjustments between each scan. Using this type of data one could calibrate this method of room temperature adjustment.

3.3.5 Flat surface topography

As shown in the previous line topographs, there is curvature in the data for samples that are meant to be flat. This is an important effect to understand for scanning because we would like to be able to scan at a constant height above this surface for magnetic imaging. Because of the geometry of the scanner design (See Figure 3.4), the scan head gets closer to the sample as it moves out in x, and farther away as it moves out in y. For this reason, when a large topograph of a flat surface is taken, it shows up as a saddle, and not a plane. A topograph of a clean sapphire surface is shown in Figure 3.14. Since it is so smooth, we can do a non-linear fit to this surface using the function $z = a + bx + cy + dxy + ex^2 + fy^2$, but with fewer data points. This is what Adam Schneider has done for the scanning software. If the magnetic sample surface is flat, like that of the sapphire sample shown, we can perform this fit and then scan the Hall probe over the sample without much height variation. However, the degree of height variation can be tested by watching the capacitance read-out of the trampoline sensor while scanning.

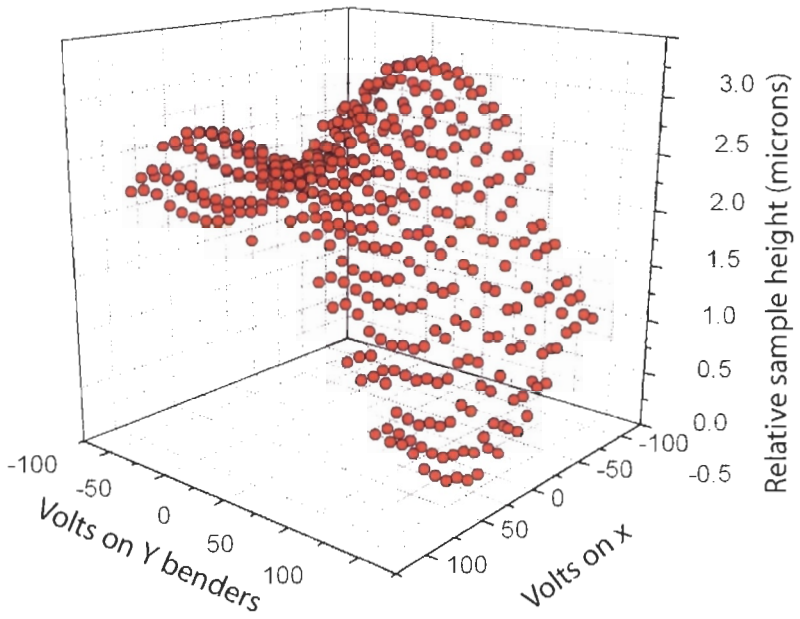

Figure 3.14: A 660×660 μm surface topograph of a clean sapphire sample showing the height change in the scan head as it scans. This surface can be fit to and then scanned over during Hall probe imaging to ensure the sensor is at a constant height above the sample.

3.4 Coarse motion

3.4.1 Three axis Attocube coarse motion system

The sample thermal stage sits on top of a stack of three x, y, z Attocube positioners designed for low temperature use, each with 7 mm of travel. They consist of two main parts: a piezo stack, which is able to expand and contract by small amounts under applied voltage, and the motion stage, which is clamped around a bar that is glued to the end of the piezo stack. The clamp is only so tight however that it takes 5 newtons of force for it to slide along the bar. This is important because the Attocubes operate using a stick-slip mechanism.

A sawtooth voltage signal is applied to the piezo stack, which enables the stage to move. In one cycle, the voltage ramps up causing the stack to expand, and the

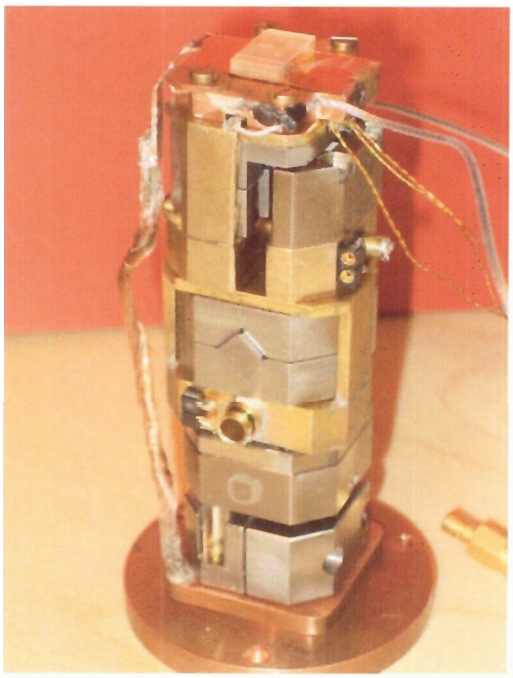

Figure 3.15: The three axis Attocube sample positioning system with capacitive read-out. Each axis has 7 mm of travel, and moves using an inertial stick-slip process instigated by a piezo stack being driven by a sawtooth signal, causing a clamp (stage) to work its way out or back along a bar on the end of the stack. The capacitive sensors are part of the brass brackets shown mounted around the x and y attocubes.

stage clamped around a bar at the end of the stack moves with it; then the voltage drops, pulling the bar back so rapidly that it slips in the clamp. Over many cycles, the clamp works its way out in steps; the size of which range from tens of nanometers to microns depending on the peak voltage of the signal. The speed of extension or retraction of the clamp is determined by the frequency of the signal. These two operating parameters are easily tuned manually on the Attocube amplifier or in a LabVIEW window on the PC, where you choose the number of steps you want to take at a given voltage and frequency.

Position read-out for the Attocubes cannot be done by simply counting steps because of the friction involved in the stick-slip process. Although the step size can

be tuned, the friction causes it to vary stochastically about an average size, making micro-navigation less and less precise as the number of steps increases.

3.4.2 Capacitive position read-out

There is a position read-out available from Attocube, which uses an optical interferometer. However, we decided to retro-fit our cubes with a homebuilt capacitive position read-out system. As mentioned, because of the stochastic nature of the stick-slip proccess, without a position read-out, it is not possible to move the sample by a precise distance by counting the number of steps taken and multiplying by an average step size. The actual position will deviate from this average in a random walk like fashion; increasing roughly as the square root of the number of steps.

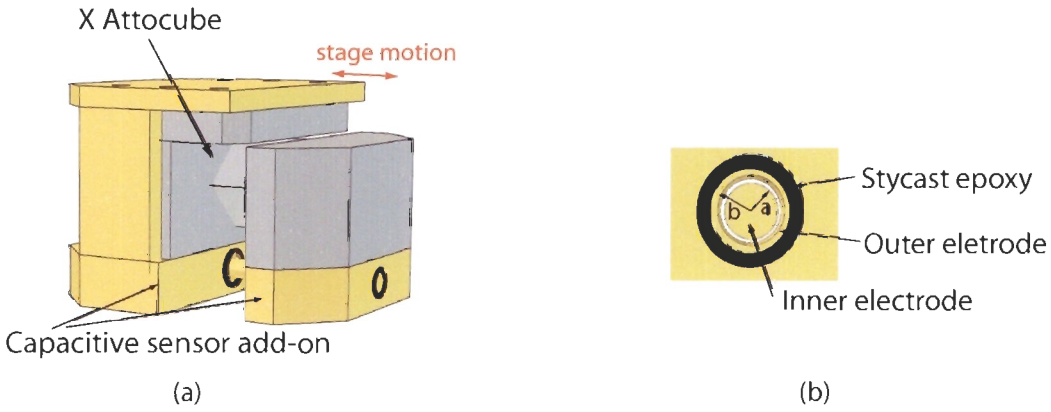

Figure 3.16: (a) The x and y Attocubes were retrofitted with coaxial capacitive sensors. (b) The variable capacitor is made up of two coaxial brass cylinders for electrodes, whose radii differ by a small amount so that one can just slide inside the other without touching. When the electrodes are well aligned, and shielded, as they are in our design, the capacitance varies linearly with the length of overlap between the two cylinders.

To address this, we used a variable coaxial capacitor developed by Taras Chouinard, in our group. It consists of two thin-walled brass cylinders whose radii differ by a small amount so that one just fits inside the other without touching. One electrode is glued

to the sliding clamp piece of the Attocube, while the other is attached to the base (see Figure 3.16). As the clamp moves, the length of overlap between the two electrodes changes, as does the capacitance. This capacitive sensor was calibrated by recording the capacitance for a number of translations, the distance of which was measured with calipers. The data are plotted in Figure 3.17, and shows that, as expected, the capacitance varies roughly linearly in distance with a linear best-fit slope of 0.4 pF/mm. A better curve fit can be done, by another student, and with the sensitivity of the A.H. capacitance bridge, repositioning of the Attocube with sub-micron precision will be achievable with this system.

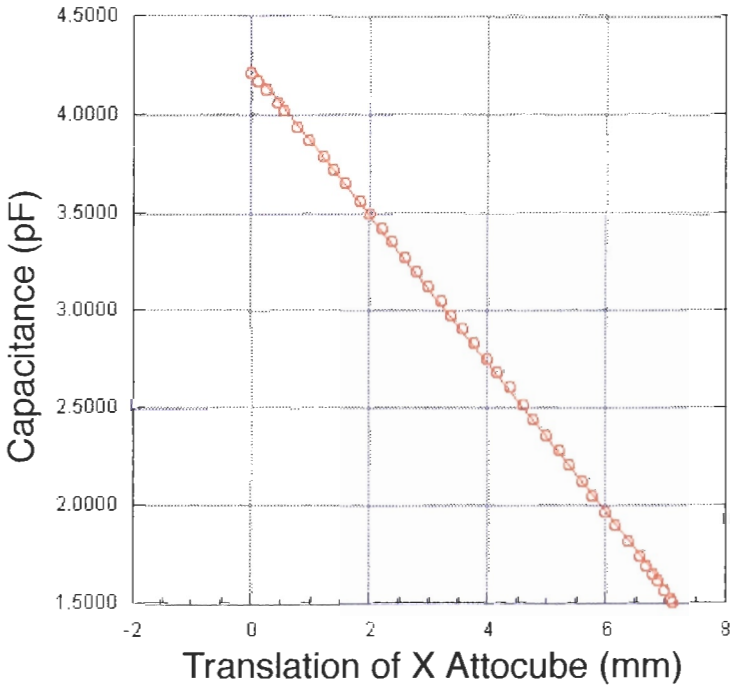

Figure 3.17: The capacitive sensor was calibrated by measuring a number of extensions of the Attocube clamp with calipers, while recording the read-out on the Andeen Hagerling capacitance bridge. Here is shown the data, with a linear fit giving a slope of 0.4 pF/mm.

This capacitor setup is a promising solution for navigating around large samples or between multiple samples with great precision. The first generation retrofit design to

the Attocubes had its glitches when cooled to liquid helium, possibly due to differential thermal contraction causing misalignment of the electrodes. However, the system did show great potential at room temperature. Taras has constructed a new coarse positioner with the capacitive sensor built in. This design should be more robust on cooling to low temperatures because of its simple design, leaving less chance for misalignment of the cylindrical electrodes.

3.5 Superconducting magnet

To create a homogeneous magnetic field for the sample, and to obtain a suitable density of vortices appropriate for imaging with SHPM, a little thought must go into the magnet design. An appropriate upper bound on the density of vortices would be one flux quantum per square micron. With this density, one could image many vortices in a single scan without being limited by the spatial resolution of the technique.

If we assume that the free space flux density B_z inside our solenoid is just redistributed in bundles in the sample, and the overall flux stays the same, then the flux through one square micron due to this field is just the flux quantum:

$$B_z \times 1\,\mu\mathrm{m}^2 = \Phi_0. \tag{3.3}$$

So the maximum field we need at the sample is

$$B_{max} = \frac{2 \times 10^{-15}\,\mathrm{Wb}}{10^{-12}\,\mathrm{m}^2} = 2\,\mathrm{mT} = 20\,\mathrm{Gauss}. \tag{3.4}$$

To achieve a homogenous field on this order, I have wound 850 turns of superconducting niobium titanium wire around the vacuum can, see Figure 3.18(b), centered on the sample. The wire has a diameter of 0.18 mm, giving us a superconducting solenoid 15 cm long with a radius of 2.8 cm. The axial field at the sample per Amp of current in the wire is therefore

$$\frac{B}{I} = \frac{\mu_0 n}{\sqrt{l^2 + 4r^2}} = 66\,\frac{\mathrm{Gauss}}{\mathrm{Amp}}, \tag{3.5}$$

using the equation for a non-infinite solenoid. The current is provided by an HP 6642A power supply operating in constant current mode. Only about 1/3 of an Amp is needed to produce the maximum field discussed above.

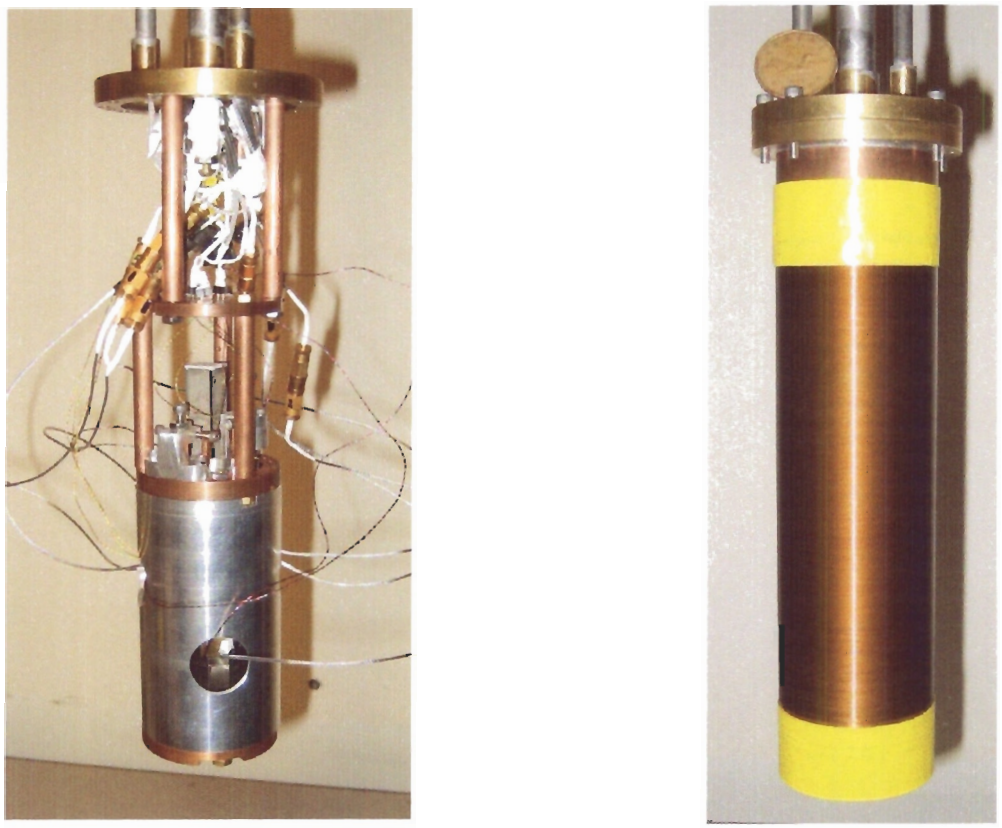

Figure 3.18: The scanning Hall probe microscope (a) goes inside the vacuum can with an 850 turn superconducting solenoid wound around it shown in (b).

Chapter 4

Thermal Design

Thermal considerations were inherent to the mechanical design of the SHPM, discussed in the previous chapter, where sound material choices needed to be made to ensure the structural integrity of the microscope and the efficient transfer of heat through it. In this chapter I will discuss some of the more specific aspects pertaining to the thermal design included in the cryostat, the sample stage, and the SHPM insert, through which the wiring goes. Proper thermal design of these components is important in having a reliable low temperature experiment.

4.1 Cryostat

For the SHPM we have built a cryostat out of old components from around the department (see Figure 4.1). The cryostat consists of a large glass nitrogen dewar for pre-cooling, which houses a smaller glass helium dewar, into which the SHPM insert fits nicely. These two dewars are mounted into a refitted cryostat rack with wheels for easy transport to other locations. The helium dewar is mounted on the underside of an aluminum plate; particular care was required here as this must be a hermetic seal so that air cannot get in and freeze out on the inside of the dewar when it is cold. To allow for good pumping and venting of the helium bath, we have made a custom collar for the top of the cryostat with a KF 50 port on it. A Stokes pump in the basement can be hooked up to this port for pumping on the bath to reach a

base temperature of 1.2 K. The SHPM insert has a flange that gets bolted to the top side of the collar, and with rubber o-ring seals on either side, the dewar is leak tight. Leak testing was standard protocol throughout the construction of the cryostat and likewise for the SHPM insert, which is under high vacuum during experiments.

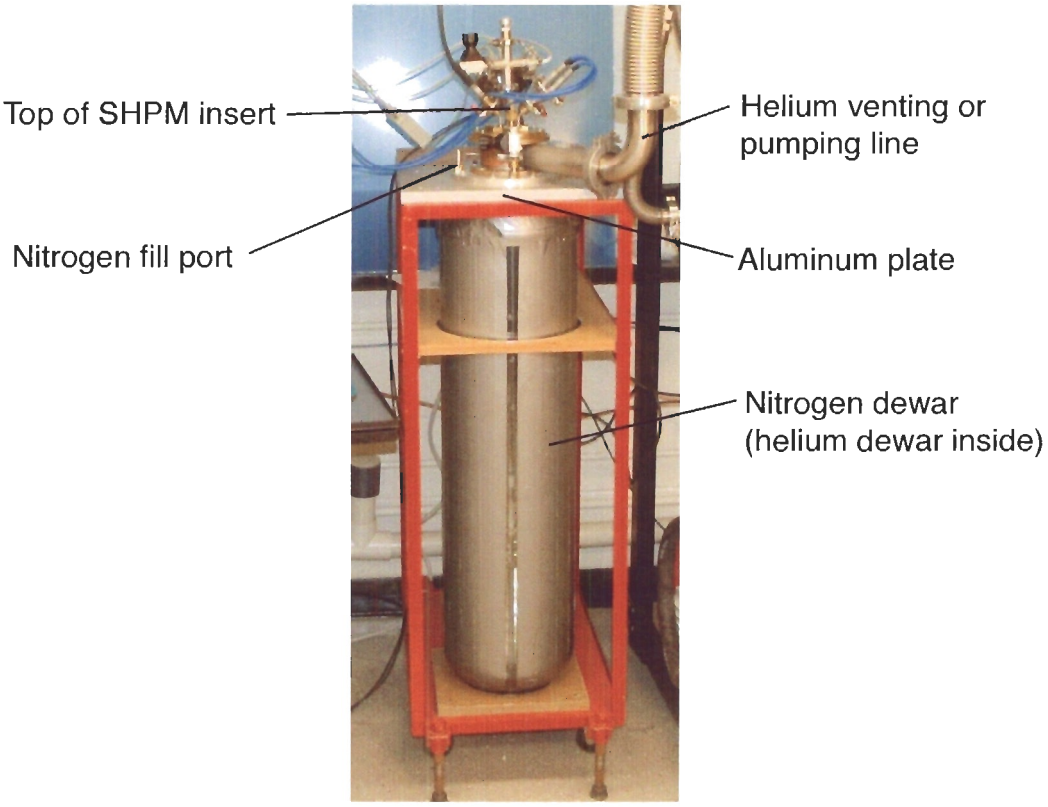

Figure 4.1: A picture of the cryostat we built for the SHPM.

The outer nitrogen dewar, or "jacket", is large for practical reasons: chief among them is that during multi-day cool-downs, refilling the liquid nitrogen will not be necessary in the middle of the night to keep the experiment cold until the following day. Furthermore, it will seldom need filling throughout the days. If, for some reason, the experiment needs to be thermally cycled in a reasonable amount of time, we have built in a means of pumping out the unused liquid nitrogen to speed up the process.

We have put two nitrogen ports into the top plate of the cryostat. Using one port, we put an over-pressure of nitrogen gas into the nitrogen space of the dewar. The liquid nitrogen is then drawn from the bottom of dewar through a tube that fits down the other port.

To apply an over-pressure in the nitrogen space of the dewar, we needed to join, and seal, the rim of the dewar to the underside of the aluminum plate. For this, we used part of a stainless steel salad bowl as a transition between the points, duct tape to seal the joint at the dewar, and a bolted glue-joint for the underside of the plate. We have also put two holes in the side of the salad bowl for extra venting while filling the dewar with liquid nitrogen. During nitrogen extraction, these holes are plugged with rubber bungs to maintain an over-pressure of nitrogen gas in the dewar.

Duct tape has found another good use in shatter-proofing the glass dewar in case of a mishap. We covered the entire nitrogen dewar with duct tape except for a viewing strip down the middle where one can look through both dewars to see the SHPM insert and most importantly, the helium level in the inner dewar.

4.2 Sample thermal stage

The sample stage was discussed briefly in the previous chapter for its mechanical design, which includes a capacitive touch-down "trampoline" sensor, allowing for sensitive topography measurements to be done with the SHPM. But of equal importance in the effective use of the SHPM are the temperature control capabilities also built into the sample stage. Because the microscope is designed primarily for the study of high temperature superconductors, which exist over a broad range of temperatures, thermal considerations were weighted heavily in the design of the sample stage. Following an overview of the bulk heat transfer away from the sample stage to the helium bath, in this section I will discuss the sample thermometry and heating and show some thermal calculations based on a simple model that indicate sound performance of this system. The system has been tested at low temperatures and works in good accordance with these calculations.

4.2.1 Heat transfer from the sample stage

The sample stage is not in direct contact with the helium bath and sits on top of the x, y, z Attocubes, which are mounted to the lowest level of the experiment, so the heat from the sample necessarily takes a long path away from the sample to the bath. To ensure good heat transfer along this path through the experiment, we have used materials with good thermal conductivity to connect the various stages. We used copper posts as stand-offs between the lid of the vacuum can and the scanning stage, and the coarse motion and sample stage are held under the scanning stage by an aluminum pipe.

The most thermally resistive elements along the heat path from the sample to the bath were the piezoceramic stacks, which are integral parts of the Attocubes. To short circuit these, I used pieces of copper braid to thermally link the base flange, on which the Attocubes sit, to the sample stage and to two other points along the positioners. The picture of Figure 4.2 shows how the thermal link is made to the copper base of the sample stage, and the others are made in a similar fashion. These thermal links are very effective in extracting the heat produced by the Attocubes when they move, as well as from the heated sample when it needs to be cooled back down.

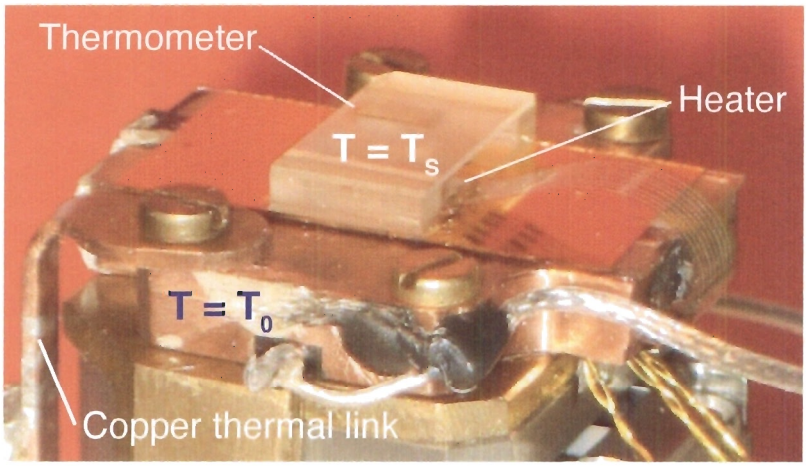

Figure 4.2: The sample stage consists of a capacitive touch-down sensor (a glass coverslip), with an open ended sapphire box on top of it, which acts as an isothermal sample platform. The temperature of this platform, and thus of the sample, is controlled using and a Cernox SD-1050 thermometer and a 1 kΩ Kapton strip heater that are glued to the inside of the box.

4.2.2 Sample thermometry and heating

Research on high T_c cuprates using our SHPM would be very limited in scope if the sample could only be at the base temperature of the liquid nitrogen or helium bath. Therefore temperature control of the sample is of paramount importance in our experiment. Accurate temperature control requires accurate thermometry, and to enable this we have used a Cernox SD-1050 thermometer[1] glued to the underside of a sapphire platform, on to which the sample is mounted. Sapphire has a high phonon thermal conductivity at low temperatures, making the sample platform essentially an isothermal structure. Measuring the temperature inside the sapphire enclosure, therefore, gives an accurate measure of the sample temperature. The 4-wire measurement is made by a Cryocon 62 temperature controller. To heat the sample, we use a 1 kΩ

[1]Cernox thermometer was purchased from LakeShore Cryotronics, Inc.

Kapton strip heater, the placement of which inside the sapphire box is important to ensure efficient and symmetric heat transfer to the sample.

Before constructing of the rather complex sample thermal stage, I calculated the power needed from the heater to hold the sample at a temperature of 100 K (the highest temperature we will routinely require), in order to provide an estimate of the maximum current required through the Kapton strip heater. Too high a current would be undesirable, possibly requiring design changes. Another quantity of interest that is affected by design parameters is the time for the sample to cool from 100 K back down to 4.2 K; this was calculated as well.

To carry out these calculations I used an approximate model of the system, assuming the sapphire platform was isothermal at temperature T_s, and the copper base, as well as the fixed ends of the cover-slip trampoline sensor, to be at the temperature of the bath T_0 (see Figure 4.2). In this model, the thermal gradient occurs only across the sections of cover-slip on either side of the sapphire platform. It is therefore simple to calculate the rate of heat transfer away from the sapphire box using the following formula:

$$\dot{Q} = \frac{2A}{l} \int_{T_0}^{T_s} \kappa(T) dT, \tag{4.1}$$

which is the equation for conductive heat transfer through a material of thermal conductivity $\kappa(T)$. A is the cross-sectional area of the cover-slip perpendicular to the heat flow, and is multiplied by two because heat flows out from both sides of the platform; and l is the length along which the heat flows. Empirical data for the thermal conductivity of pyrex glass was found in [36], and the integral involving $\kappa(T)$ from $T_0 = 4.2$ K to $T_S = 100$ K is approximately 305 mW/cm. Taking our final design parameters, $A = 1.8 \times 10^{-}2$ cm^2 and $l = 0.7$ cm, as an example, the heat flow, and thus the maximum Joule heating needed by the heater is

$$\dot{Q} = I_{max}^2 R = 15.7 \text{ mW}. \tag{4.2}$$

And since the resistance of the heater is $\sim$1 kΩ, the maximum current required to keep the sample at 100 K is

$$I_{max} \approx 4 \text{ mA}$$

in this approximation, well within design constraints.

To calculate, in the absence of heat, the cooling time of the sample from $T_i = 100$ K to $T_f = 4.2$ K, we start with the time derivative of the first law of thermodynamics,

$$\frac{dU}{dt} = -\dot{Q}$$

where U is its internal energy of the sapphire box, and $\dot{Q}$ is again the heat flow through the cover-slip. Using the chain rule on the left hand side, we have

$$\frac{dU}{dT_s}\frac{dT_s}{dt} = -\dot{Q}. \tag{4.3}$$

But dU/dT_s=$C_v(T_s)$ is just the heat capacity of the sapphire box at temperature T_s. We can substitute this into the above equation, and rearrange to obtain

$$\frac{dT_s}{dt} = -\frac{\dot{Q}(T_s)}{C_v(T_s)}. \tag{4.4}$$

The cooling time is then

$$\Delta t = \int_0^t dt' = \int_{T_f}^{T_i} \frac{C_v(T_s)}{\dot{Q}(T_s)} dT_s. \tag{4.5}$$

It is useful to first take the simple example of a metallic stage at low temperature, where $\kappa(T) = \kappa_0 T$ and $C_v(T) = \gamma T$. In this case, the thermal conductivity integral of Eq. 4.1 becomes

$$\dot{Q} = \frac{2A}{l}\int_{T_0}^{T_s} \kappa(T) dT = \frac{A\kappa_0}{l}(T_s^2 - T_0^2), \tag{4.6}$$

and so the cooling time is

$$\Delta t = \frac{\gamma l}{A\kappa_0}\int_{T_f}^{T_i} \frac{T_s dT_s}{(T_s^2 - T_0^2)}. \tag{4.7}$$

Since the base temperature is much smaller than the sample temperature for most of its range, we can neglect T_0, and the cooling time is simplified to

$$\Delta t = \frac{\gamma l}{A\kappa_0}\int_{T_f}^{T_i} \frac{dT_s}{T_s} = \frac{\gamma l}{A\kappa_0}\ln(\frac{T_i}{T_f}). \tag{4.8}$$

Solving for the final temperature here shows that it is an exponential decaying function of time,

$$T_f = T_i \exp(-\frac{A\kappa_0 \Delta t}{\gamma l}), \tag{4.9}$$

In this simple situation, the characteristic decay time is $\tau = \frac{\gamma l}{A\kappa_0}$.

In our case we can solve for the cooling time more accurately by using thermal properties characteristic of the glass and sapphire used to construct the thermal stage. In the temperature range 4 K to 100 K, the thermal conductivity integral of pyrex glass is $\Theta(T) \approx \Theta_0 T^{3/2} = 0.03\, T^{3/2}$ W/m [36]. For the sapphire box, which has a mass of 0.5 g, the heat capacity is $C_v \approx C_0 T^3 = 8 \times 10^{-8} T^3$ J/K in the same temperature range. We can now evaluate the cooling time using Eq. 4.5 to be

$$\Delta t = \frac{C_0 l}{2A\Theta_0} \int_{T_f}^{T_i} \frac{T_s^3 dT_s}{T_s^{3/2}} = \frac{C_0 l}{5A\Theta_0}(T_i^{5/2} - T_f^{5/2}). \tag{4.10}$$

Neglecting the final base temperature, which is small compared with T_i, the cooling time is

$$\Delta t \sim 200 \text{ s},$$

which is in very good accord with experimental observation.

4.3 SHPM insert design

The insert holding the SHPM and the vacuum can was designed and built by David Broun and Patrick Turner, both of whom have past experience building low temperature inserts. The lid of the vacuum, to which the SHPM is connected, is held about 2.5 ft below the top flange of the insert by four pieces of stainless steel tubing. This tubing provides structural integrity to the insert and acts as conduit for the wiring to be brought down from the connectors at the top of the insert to the components of the SHPM. Stainless steel is a good material to use here for its low thermal conductivity, minimizing the heat-leak from the top of the insert, which sits in the lab at room temperature. I have added three copper baffles along the tubing to help break up the convection of the helium vapor above the bath, thereby making the most of its cooling power on the tubing and reducing helium boil-off in the process.

The high voltage wires for the scanner are brought down the central tube, while those for the capacitance, thermometry and heating, Hall probe, and the coarse motion are brought down the other tubes. Since the wires are coming from room temperature, they needed to be heat-sunk before going to any of compenents, whose operation rely on this, particularly for temperature control, where we want to measure the temperature of the sample, not the ends of the wires. For heat sinking, we fixed copper bobbins to the underside of the lid of the vacuum can and wrapped each wire tightly around them about 10 times. To ensure good thermal contact between the wire wrap and the bobbin, we first wrapped the bobbin with a piece of thin paper soaked in GE varnish. More importantly, however, we ensured good thermal contact between the bobbins and the brass lid. To do this, we put through holes down the central axes of the copper bobbins and then used brass bolts to attach them to the lid. Brass has a larger thermal contraction than copper, causing the bobbins to be pressed onto the underside of the lid upon cooling down.

Chapter 5

Scanner electronics and software

The electronics necessary for the operation of the SHPM come from a combination of commercially available and home built instruments. Communication with these instruments for such things as scanning, sensor touch-down, and temperature control is made possible using LabVIEW, the programming of which was done in large part by Adam Schneider, a recent undergraduate group member. Figure 5.1 is a schematic outlining our electronic design. The instruments are mounted in a rack beside the cryostat and are connected to the computer with GPIB cables where possible. In this chapter I will describe the electronics used for the different components of the SHPM.

5.1 Scanner electronics

To apply voltages to the piezos of the x, y, z fine motion, we use three channels on a 16 bit National Instruments D/A card installed in our Dell PC. This analog output has a range of only 0–10 V. To obtain the large voltages necessary to drive the piezo benders, we have had a custom amplifier built by the SFU electronics shop. The single input from the D/A card is output from the amplifier as two signals symmetric about ground. The amplifier has three gain settings, with a maximum of gain of 30, capable of producing a 600 V differential signal for low temperature use. An interlock can also be set at 100, 300, and 600 V to protect the piezo elements from depolarization at room temperature.

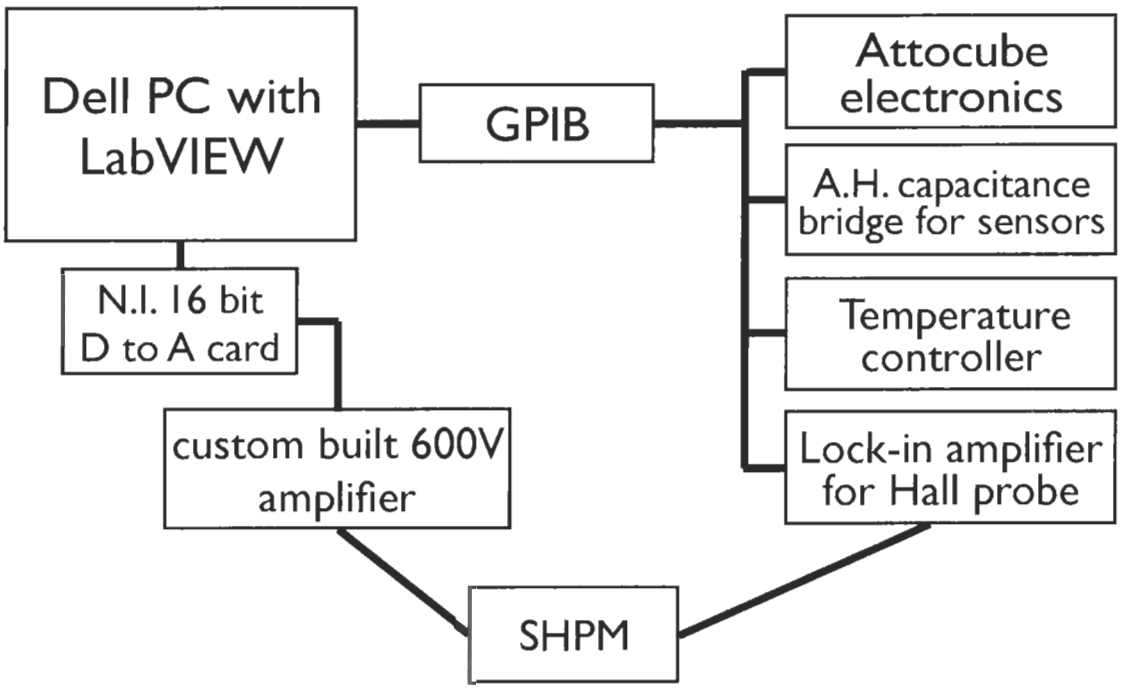

Figure 5.1: A schematic of the electronics for the SHPM.

5.2 Thermometer and heater electronics

To measure the temperature of the sample, we perform a 4 wire measurement on a Cernox SD 1050 thermometer. It was calibrated using the SQUID magnetometer setup at UBC. The calibration curve was downloaded onto a Cryocon 62 temperature controller. Heating is done by passing a current from the Cryocon, through a 1000 Ω kapton strip resistor. After power settings are taken for the heater at various temperatures, the Cryocon can do its job and precisely control the temperature of the sample throughout our range of interest.

5.3 Attocube electronics

To drive the Attocube anp100 x,y,z coarse positioning system, we purchased an amplifier from Attocube Systems that outputs a sawtooth signal of varying amplitude, and frequency. This has LabVIEW drivers that we have incorporated into programs for the sample approach, cool-down motion, and sample repositioning with feedback from the capacitive sensors.

5.4 Capacitive sensor electronics

The capacitance measurements are taken using an Andeen Hagerling bridge. For optimal measurement precision, the bridge requires that each capacitor electrode be connected using the center conductor of a coax line; in addition, the outer conductor of the line, as well as the surroundings of the electrode are grounded. Since we have three capacitive sensors the touch-down trampoline, and the two coax position sensors on the Attocubes we purchased a multiplexor, which allows us to switch between measurements of the three.

5.5 Hall probe electronics

We have used a Stanford SR-810 DSP lock-in amplifier for the bias current and the Hall voltage measurement. The bias current is taken from the sine out on the lock-in, which is a voltage output. For the Hall probe to operate, the bias current must be of the order of 10 μA. To convert the voltage output to the required current source I have put in a 220 kΩ resistor in series with the sine out. As discussed in Chapter 2, a bias voltage can be put onto the gate lead of the Hall probe to optimize the noise in the device. For this I have made a box with a battery and a voltage divider, including a 10 turn pot resistor. This provides a bias voltage which is very stable, and ranges from 0 to 0.5 V.

5.6 Scanning software

The programming was all done in LabVIEW and for the most part by Adam Schneider. He used the feedback from the capacitive sensors and communicated with the large area scanner and the Attocubes to make important VIs enabling key functions of the SHPM. Those that involve feedback from the capacitive sensors include the surface topography and calibration, and the micropositioning of the Attocubes. A particularly important VI that is used frequently for topography and magnetic imaging is one that automates the coarse approach of the sample towards the tip or Hall probe, stopping it as soon as it touches softly. This allows one to manually position the sample a safe distance away, and then let the program do the rest. He also programmed a self-contained console for the scanning magnetic imaging with a number of user input parameters including x, y scan ranges, scan height above the sample and scan angle. An integral part of the scanning software is the fitting algorithm for the scan surface. As mentioned earlier, to scan at a constant height over a flat surface, the z position of the sensor needs to be scanned over a saddle-like surface as a function of its x, y position. Adam programmed a fitting algorithm that occurs before each scan to accomplish this.

Chapter 6

Preliminary results and discussion

The last part of my work involved the wiring up of a 150 nm Hall probe, calibrating it in a dip probe, and then imaging magnetic fields with it. Before carrying out these tasks however, a carrier chip needed to be fashioned for the Hall probe. The carrier chip is an intermediate point of strain relief for the wires connecting to the Hall probe, and thus needs to have five isolated conducting pads, matching the number of contacts on the Hall probe. The chip must also have good thermal conductivity to ensure the Hall probe can dissipate as much heat as possible produced by the bias current. To meet this objective, we chose to use a piece of intrinsic semiconductor wafer and evaporate the gold contacts on to it. A thin layer of chromium ~100 nm was evaporated first as an adhesion layer, and then at least 500 nm of gold was added on top, sufficient for wire-bonding to. The first chips I made in this way seemed promising, but it turned out that the silicon wafer I used, obtained from Dr. Mike Thewalt, was conducting enough to short the contact pads, making these carrier chips unusable. Subsequent attempts were made with this procedure using an insulating semiconductor substrate, but in these cases the wire-bonding did not take consistently to the pads of the carrier chip. Wire-bonding to the Hall probe contacts also proved inconsistent. In the end, instead of the evaporated gold pads, I used five miniature conducting pads from a flexible edge connector, stuck down with GE varnish. The wire-bonding was also abandoned, and I used silver epoxy for both the carrier chip and the Hall probe. Shown in Figure 6.1 is the carrier chip with the Hall probe mounted

onto the scanning head of the SHPM.

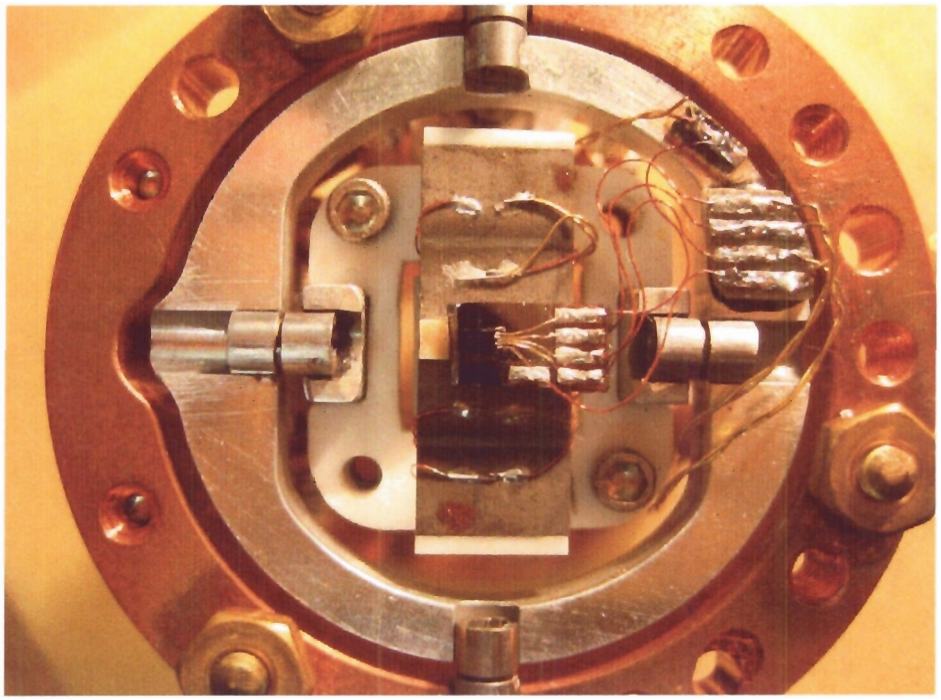

Figure 6.1: Picture of the scanner with Hall probe mounted.

The 150 nm Hall probe, now mounted on the carrier chip, was first calibrated using a copper solenoid in a dip probe at 77 K to obtain a Hall coefficient of $R_H = 0.24\ \Omega/\mathrm{G}$. This was with a bias current of 4 μA, and a gate voltage of 150 mV. Hall probe was then mounted on to the SHPM, and we were able to cool the scanner to 77 K and obtain images of a magnetic structure on a high density floppy disk shown in Figure 6.2. Although there is clearly magnetic structure in the image, the vertical stripes seem to be wider than bits, which are usually the order of a couple microns for these types of disks. For the next tests, to be carried out by Ricky Chu in our group, we have some garnet film samples. The magnetic structures in garnet films, known as "worm-domains", are of the order of $\sim 5\mu$m, and are thus ideal for imaging with scanning Hall probe microscopy. We are also able to image these samples using Dr. Bret Heinrich's magneto-optical microscope, giving us something to compare our SHPM images with.

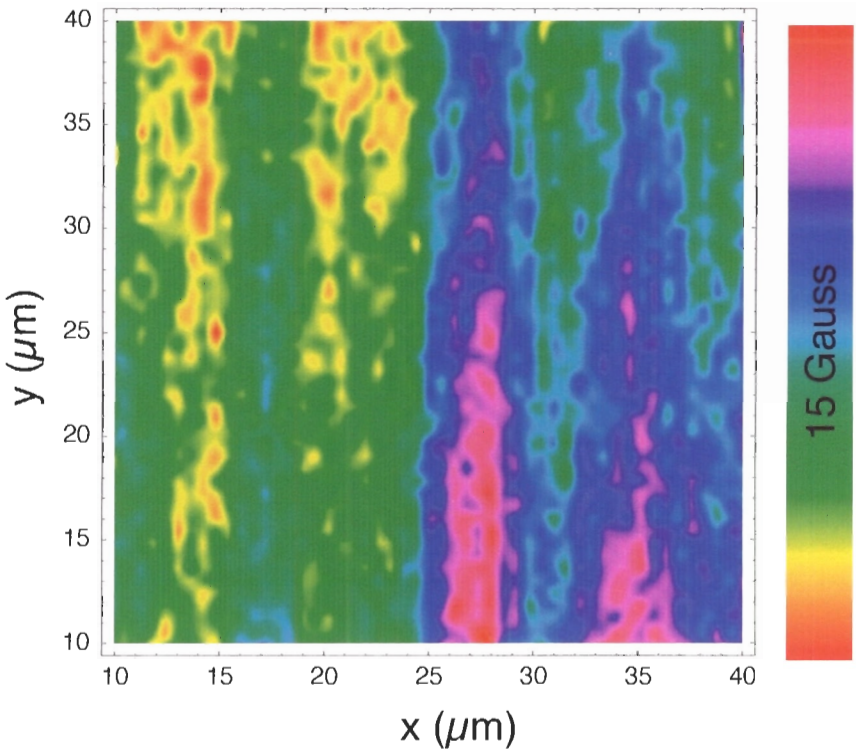

Figure 6.2: Scanning Hall probe image of a floppy disk at 77 K taken with a 150 nm Hall probe. This scan has 2500 pixels, and took approximately 10 minutes to complete.

During this thesis work I designed, built and characterized many components of this scanning Hall probe microscope. To start with, I built a large-range cryogenic dual S-bender scanner for the Hall probe to be mounted on. Although this design had already been demonstrated [3], I commissioned a custom high voltage amplifier to be built, and using this established that at low temperatures the piezos could be driven at a significantly higher voltage than was demonstrated in [3]. This allows for the length of the scanner to be shorter, thereby increasing the resonant frequency without compromising scan-range.

Another key component of the SHPM, which I designed and built, is a sample stage that has built-in temperature control and a capacitive touch-down sensor. Without

STM feedback in our SHPM, this capacitive sensor, with ~ 2 nm deflection sensitivity, is indispensable for high-resolution SHPM imaging, and for our automated sample approach. I used this sensor to carry out topographical imaging in the characterization, and calibration of the scanner at room temperature, 77 K, and 4.2 K. During the some of these cool-downs of the SHPM, I also tested the temperature control capabilities, which worked according to design. Finally, I wired up a Hall probe, as discussed above, and obtained a low-temperature magnetic image of a floppy disk. There is, however, still room for some improvements to be made to optimize the performance of this SHPM

The Hall probe we used in the initial proof-of-principle tests was not polished to minimize the height of the active region above the sample surface. We do however have the tools and the technique to do this, so I think the next step will be to properly polish a Hall probe, which will bring the sensor closer to the sample optimizing spatial resolution. Furthermore, in this case, the fit to the sample surface will be more representative of the surface directly under the Hall sensor.

Bibliography

[1] Binnig, G., Rohrer, H., Gerber, C. & Weibel, E. Surface studies by scanning tunneling microscopy. *Physical Review Letters* **49**, 57 (1982).

[2] Binnig, G., Quate, C. F. & Gerber, C. Atomic force microscope. *Physical Review Letters* **56**, 930 (1986).

[3] Siegel, J., Witt, J., Venturi, N. & Field, S. Compact large-range cryogenic scanner. *Review Scientific Instruments* **63**, 2520 (1995).

[4] Hicks, C. W., Luan, L., Moler, K. A., Zeldov, E. & Shtrikman, H. Noise characteristics of 100 nm-scale GaAs/$Al_xGa_{1-x}As$ scanning hall probes. *Unpublished* (2006).

[5] Hess, H. F., Robinson, R. B., Dynes, R. C., J. M. Valles, J. & Waszczak, J. V. Scanning-Tunneling-Microscope observation of the Abrikosov Flux Lattice and the density of states near and inside a fluxoid. *Physical Review Letters* **62**, 214 16 (1989).

[6] Chang, A. M. *et al.* Scanning Hall probe microscopy. *Applied Physics Letters* **61**, 1974 6 (1992).

[7] Davidović, D. *et al.* Correlations and disorder in arrays of magnetically coupled superconducting rings. *Phys. Rev. Lett.* **76**, 815 18 (1996).

[8] Oral, A., Bending, S. J. & Henini, M. Real-time scanning Hall probe microscopy. *Applied Physics Letters* **69**, 1324 6 (1996).

[9] Oral, A. *et al.* Direct observation of melting of the vortex solid in $Bi_2Sr_2CaCu_2O_{8+\delta}$ single crystals. *Physical Review Letters* **80**, 3610 3 (1998).

[10] Vu, L. N., Wistrom, M. S. & Harlingen, D. J. V. Imaging of magnetic vortices in superconducting networks and clusters by scanning SQUID microscopy. *Applied Physics Letters* **63**, 1693 5 (1993).

[11] Kirtley, J. R. *et al.* High resolution sanning SQUID microscope. *Applied Physics Letters* **66**, 1138 40 (1995).

[12] Stawiasz, K. G., Ketchen, M. B. & Narasimhan, L. R. White noise performance of integrated DC SQUID susceptometers in high magnetic fields. *IEEE Transactions on Applied Superconductivity* **5**, 3230 2 (1995).

[13] Hasselbach, K., Veauvy, C. & Mailly, D. MicroSQUID magnetometry and imaging. *Physica C* **332**, 140 7 (2000).

[14] Deng, Z. *et al.* Metal-coated carbon nanotube tips for magnetic force microscopy. *Applied Physics Letters* **85**, 6263 (2004).

[15] Guikema, J. W. *Scanning Hall Probe Microscopy of Magnetic Vortices in Very Underdoped yttrium-barium-copper-oxide* (PhD Thesis, Stanford University, 2004).

[16] Bending, S. J. Local magnetic probes of superconductors. *Advances in Physics* **48**, 449 535 (1999).

[17] Winkler, A. *et al.* Magnetic force microscopy sensors using iron filled carbon nanotubes. *Journal of Applied Physics* **99**, 5 (2006).

[18] Chang, J. *et al.* Magnetic state control of ferromagnetic nanodots by magnetic force microscopy probe. *Journal of Applied Physics* **100**, 104304 (2006).

[19] Guarisco, D. & Nguy, H. High linear density in perpendicular recording. *Journal of Applied Physics* **93**, 6745 (2002).

[20] Kirtley, J. R. SQUID microscopy for fundamental studies. *Physica C* **368**, 55 65 (2002).

[21] Kirtley, J. R. *et al.* Direct imaging of integer and half-integer Josephson vortices in high-T_c grain boudaries. *Physical Review Letters* **76**, 1336 9 (1996).

[22] Björnsson, P. G. *Low-Temperature Scanning Magnetic Probe Microscopy of Exotic Superconductors* (PhD Thesis, Stanford University, 2005).

[23] Gardner, B. W. *et al.* Manipulation of single vortices in $YBa_2Cu_3O_{6.354}$ with a locally applied magnetic field. *Applid Physics Letters* **80**, 1010 2 (2002).

[24] Hicks, C. W. High resolution scanning GaAs/Al_xGa_{1-x}As Hall probes. *APS March Meeting presentation* (2006).

[25] Pearl, J. Structure of superconductive vortices near a metal-air interface. *Journal of Applied Physics* **37**, 4139 41 (1966).

[26] Wynn, J. C. *et al.* Limits on spin-charge separation from $hc/2e$ fluxoids in underdoped $YBa_2Cu_3O_{6+x}$. *Physical Review Letters* **87**, 197002 (2001).

[27] Abrikosov, A. A. *Type II Superconductors and The Vortex Lattice* (Nobel Lecture, December 8, 2003).

[28] Ginzburg, V. L. & Landau, L. D. *Zh. Eksp. Teor. Fiz.* **20**, 1064 (1950).

[29] Tinkham, M. *Introduction to superconductivity* (McGraw-Hill, 1996).

[30] Anderson, P. W. The resonating valence bond state in La_2CuO_4. *Science* **48**, 449 535 (1987).

[31] Senthil, T. & Fisher, M. P. A. Z_2 gauge theory of electron fractionalization in strongly correlated systems. *Physical Review B* **62**, 7850 81 (2000).

[32] Liang, R. *et al.* Preparation and characterization of homogeneous YBCO single crystals with doping level near the SC-AF boundary. *Physica C* **383**, 1 7 (2002).

[33] Bonn, D. A. *et al.* A limit on spin-charge separation in high-T_c superconductors from the absence of a vortex-memory effect. *Nature* **414**, 887 9 (2001).

[34] Senthil, T. & Fisher, M. P. A. Fractionalization in the cuprates: detecting the topological order. *Physical Review Letters* **86**, 292 5 (2001).

[35] Senthil, T. & Lee, P. A. Cuprates as doped $U(1)$ spin liquids. *Physical Review Letters* **86**, 292 5 (2004).

[36] Corruccini, R. J. & Gniewek, J. J. *Thermal Expansion of Technical Solids at Low Temperatures: a Compilation from the Literature* (National Bureau of Standards, 1961).

[37] Grigorenko, A. N., Bending, S. J., Gregory, J. K. & Humphreys, R. G. Scanning Hall probe microscopy of flux penetration into a superconducting $YBa_2Cu_3O_{7-\delta}$ thin film strip. *Applied Physics Letters* **78**, 1586 8 (2001).

[38] London, F. & London, H. The electromagnetic equations of the supraconductor. *Proc. Roy. Soc.* **A149**, 71 (1935).

[39] Nakai, N. *et al.* Ubiquitous v-shape density of states in a mixed state of clean limit type II superconductors. *Physical Review Letters* **97**, 4 (2006).

[40] Senthil, T. & Fisher, M. P. A. Detecting fractions of electrons in the high-T_c cuprates. *Physical Review B* **64**, 214511 (2001).

[41] Uemura, Y. J. *et al.* Universal correlations between T_c and n_s/m^* (carrier density over effective mass) in high-T_c cuprate superconductors. *Physical Review Letters* **62**, 2317 (1989).

[42] Waldram, J. R. *Superconductivity of metals and cuprates* (IOP publishing LTD, 1996).